

# Investigating Chromium, Manganese, Calcium and Nickel Abundances in SN1604

Mircea Adrian Posoiu

March 21, 2013

Supervisor: Dr. Jacco Vink

Master Thesis

Utrecht University

---

## Contents

<b>1</b>	<b>Introduction</b>	<b>3</b>
<b>2</b>	<b>Theoretical Background</b>	<b>5</b>
2.1	Iron Peak Element Nucleosynthesis . . . . .	5
2.2	SN 1604 - Kepler's SNR . . . . .	7
2.3	The Datasets . . . . .	11
<b>3</b>	<b>Data Analysis</b>	<b>12</b>
3.1	Full Spectrum Analysis . . . . .	12
3.2	Regions of Interest . . . . .	20
3.3	Principal Component Analysis . . . . .	24
3.4	Analysis of Secondary Dataset . . . . .	30
<b>4</b>	<b>Discussion and Conclusions</b>	<b>32</b>

## Abstract

The purpose of this study is to investigate the abundance distribution of specific elements throughout the volume Kepler's SNR, using an extensive dataset from the Chandra observatory archive. Manganese and chromium were used to determine an estimate of the metallicity parameter that characterized the progenitor star by way of the free neutron flux released after the explosion. The resulting value,  $Z = 0.082_{-0.047}^{+0.061}$ , placed the progenitor into the solar or supersolar metallicity categories. Furthermore, abundances of calcium and nickel were computed in key regions of the remnant. Higher calcium concentrations were identified at higher radii, as a result of the environment's enrichment with alpha particles from cosmic rays. For the determination of nickel abundances, an additional dataset was employed, taken from the XMM-Newton archive.

# 1 Introduction

Supernova remnants are widely regarded as key focal points in astronomical research, both due to their importance in the field of cosmology, as well as due to the exotic thermonuclear reactions that they house. Throughout the past decades, scholars have looked at these structures from the standpoint of isolated objects in space, ultimately tying in their impact on the evolution of the universe as a whole. The extensive exploration of a large number of individual candidates has led to a rigorous classification of supernovae, according to their genesis and composition. Regardless of the increased level of understanding already achieved, the observed remnants remain objects of major interest in ongoing research. Currently, supernovae are employed in a multiple of roles across various fields of astronomy.

On the one hand, they serve as standard candles that aid in the measuring of extragalactic distances. Due to the homogeneity of type Ia supernovae, brought about from the common detonation conditions and mechanisms shared by all candidates in this subcategory, it is possible to obtain a measurement of the effective brightness of one such object, which can be then compared to the observed brightness in order to provide a distance estimate. In terms of cosmological measurements, where variable stars can no longer be employed as standard candles, the existence of supernovae allows for the mapping of large scale structures in the Universe.

Furthermore, supernovae are known to be responsible for the creation of heavy elements within our universe, as a result of the high amounts of energy released during the explosion. Nucleosynthesis that takes place inside the stellar core can only fuse elements up to and including iron atoms, due to the large binding energy of the latter. The exothermic nature of iron fusion makes it unlikely for it to occur outside of specific scenarios where a large excess of energy is input into the system. A super-

nova explosion constitutes one such case. The favorable temperature conditions that are attained within the span of a few seconds from the detonation trigger allow for the production of elements leading up to uranium, with certain mechanisms even able to briefly synthesize transuranium elements. Upon expansion and interaction with the interstellar medium, the supernova remnant contributes to an enrichment of the heavy elements abundance in the universe.

Despite the thorough investigations concerning the nature and evolution of a supernova, little is currently known regarding the progenitors of these fascinating structures. Several observational constraints have impeded a sufficiently deep analysis of the phenomenon, with additional hindering issues present in specific cases. Due to their exotic quality, supernovae explosions are a rare physical occurrence. An approximate average of such explosions within our own galaxy rates them at less than one event per century, with the latest being recorded in the year 1680. The most recent detection of a supernova within our general vicinity took place in 1987, following an explosion within the Tarantula Nebula in the Large Magellanic Cloud. Moreover, direct observations of the supernova mechanisms can only occur within a limited time frame, driven by the relatively fast reactions that determine its evolution. Unlike in most astronomical observations, where changes within short durations of time are negligible or inexistent, the window for detecting and analyzing a supernova is only open for intervals ranging from weeks and up to a few months. In cases where direct observation was inaccessible, the information regarding the supernova explosion is derived purely from the study of the resulting remnants, with limited knowledge of the progenitor star.

An added discrepancy exists between the members of different supernovae classifications that makes some candidates easier observation targets when compared to others. Specifically, Type II explosions take place following the core collapse of a massive star, above the threshold

of  $8 M_{\odot}$ . The presence of this very luminous progenitor can be detected prior to the detonation itself, allowing for a better preparation in expectation of the event. The same principle does not apply for Type Ia supernovae. The latter are generated from the gradual accretion of mass on a carbon-oxygen white dwarf, or from the gravitational interaction of a double degenerate system. Unlike the previous case, where a massive star is easily detectable in the optical range, the white dwarf progenitors of Type Ia supernovae are faint objects which cannot be recorded prior to the explosion itself.

The issue is further augmented by the fact that Type Ias store very little information regarding their initial progenitor star, making it very difficult to ascertain their nature beyond theoretical considerations. The reason for this behavior, recently coined as "stellar amnesia" (Badenes 2008), stems from the same set of properties that makes these supernovae excellent cosmological standard candles. The explosion of the white dwarf occurs at similar pressure and temperature conditions, upon accreting sufficient material to reach the Chandrasekhar mass limit. Upon the explosion of the carbon-oxygen core, a chain of thermonuclear reactions takes place, ultimately resulting in an intense increase in luminosity, as well as the creation of a fast moving shock front. The similarity between both the initial triggering conditions and the mechanisms that occur in the actual detonation make Type Ia supernovae a very homogenous group in terms of their internal properties, with little relation to the nature of their progenitors.

Recent studies in the field have attempted to unravel the mystery of Type Ia progenitors by conducting detailed analysis of the chemical composition of their remnants. In particular, by looking at specific element concentrations and concentration ratios in their current stage of evolution, it may be possible to infer estimates of the progenitor star's metallicity at the start of its evolution, prior to it becoming a white dwarf.

In particular, the presence of argon and iron peak elements (Cr, Mn, Co, Ni) might hold the key in determining the nature of remnant's parent star. The impact of metallicity variations on the peak luminosity of SNe Ia was determined by investigating the production of such elements due to the neutron excess released during the supernova explosion (Timmes 2003). Endothermic reactions that were previously infeasible during the process of stellar evolution are favored by the explosive nucleosynthesis, mainly due to the high energy output involved. Although a certain amount of iron peak elements can be created during conventional stellar nucleosynthesis, nuclear fission enables the production of a higher concentration of nickel, chromium and manganese. By focusing on the decay of the unstable  $^{56}\text{Ni}$  isotope during the burn to nuclear statistical equilibrium, it was demonstrated that there exists a linear dependency between the mass of  $^{56}\text{Ni}$  and the initial metallicity  $Z$  of the white dwarf progenitor.

A more recent investigation sought to determine the metallicity parameter by making use of the mass concentration ratio between the manganese and chromium found in the supernova ejecta (Badenes 2008). By gauging the spectral lines associated with the two elements, it was possible to obtain a measurement of the neutron excess present in the white dwarf material prior to the explosion. This is facilitated by the varying response of manganese and chromium to the aforementioned excess. On the one hand, an abundance of free neutrons in the environment facilitates the production of the  $^{55}\text{Mn}$  isotope, making the latter highly sensitive to the excess. Conversely, chromium synthesis is unaffected by the presence of free neutrons. Thus, investigating the mass ratio between the two provides a way to single out the effects of the neutron excess and to determine an estimate for the white dwarf progenitor's metallicity.

The aim of this particular study is to perform a spectral analysis of SN 1604, Kepler's supernova remnant, using a series of high quality x-ray observations taken by the Chandra

and XMM-Newton space telescopes. Of particular interest is the strength of the argon and nickel line complexes, as well as the distribution of manganese-to-chromium abundance ratios throughout the object’s volume. The analysis will seek to map out these specific element profiles and link them to the asymmetries of the

more pronounced Fe L, Si L and Fe K lines. The correlations will hopefully provide more insight into the overall nature of Kepler, its origin and the mechanisms that contributed to its evolution, in an attempt to bring the community one step closer to solving the last puzzles surrounding this peculiar supernova remnant.

## 2 Theoretical Background

### 2.1 Iron Peak Element Nucleosynthesis

Supernovae explosions are responsible for the enrichment of the raw interstellar medium with heavy elements that would not otherwise be produced without the massive energy input released during the explosion. After being constrained by the endothermic nature of iron fusion for timescales of the order of Gyr, a series of exotic reactions arise and give birth to new chemical elements within seconds of the explosion. In order to overcome the energy requirement, as well as the heightening of the Coulomb barrier - an increase in the repulsive force between protons and electrons that is favored by the higher number of protons in the nuclei - heavier elements are produced almost exclusively via neutron capture processes.

The latter are split into two categories, known as the slow s-process and the rapid r-process. The distinction is made according to the difference in neutron capture and beta decay timescales for each specific particle. The excess neutral particles released into the circumstellar medium in the initial stages of the supernova explosion accumulate onto the nuclei of the existing species. In the s-process, the neutron capture parameter  $\tau_n$  is significantly higher than the decay timescale  $\tau_\beta$ , meaning that at most one neutron can be adjoined to the nucleus prior to the emission of the beta particle. During this radioactive decay, a neutron is converted into a proton, thus increasing the atomic number of the element and giving birth to a heavier compound. In order for an even more complex element to be formed, another neu-

tron needs to be captured from the surrounding medium (Cowan & Thielemann 2004). This mechanism is more often encountered in the terminal burning stages of intermediate mass stars rather than in supernovae and, due to its nature, has a lower limit of the atomic number of the elements it can produce.

The r-process occurs in the event of a very high neutron flux, in which it is possible to reach values of  $\tau_n$  that are below  $\tau_\beta$ . In this particular case, several neutrons can be bound to the nucleus before the first beta decay occurs, allowing for a better transition on the atomic number ladder. This mechanism is made possible almost exclusively by supernovae explosions. Therein, even after the neutron flux is exhausted, these nuclei will decay towards a stable state, allowing for the formation of even heavier elements. (Cowan & Thielemann 2004).

Nonetheless, there are several other factors that interfere with the process, making it less than straightforward. The high temperature values that are associated with the high neutron emission also contribute to the release of highly energetic gamma rays. Interactions between these gamma rays and the unstable nuclei often lead to neutrons being ejected back into the medium, acting opposite to the capture mechanism. Thus, the balance between temperature and neutron capture dictates how feasible the formation of certain isotopes is within the supernova environment.

Another hindrance is presented by the incoming neutrino flux that may cause particles to undergo spontaneous beta decay. By contributing to the excitation energy of unstable nuclei, neutrino bombardment may trigger fission by increasing this parameter past a critical thresh-

old. The addition of this mechanism also requires a higher flux and, in turn, a lower  $\tau_n$  in order to properly exhibit the r-process.

The nature and quantities of elements produced during supernova nucleosynthesis also depend on the progenitor star. Different compositions of the stellar material and of the circumstellar matter lead to particular sets of fission reactions following the explosion itself. A particular interest for this paper lies in the formation iron peak elements, as a means of using their currently observed abundances in order to backtrace the evolution of the remnant up to its progenitor phase. These elements can be synthesized either during the final burning stages of large stars, where they will be expelled into the medium by the supernova explosion, or during the neutron capture processes described above.

The production of these elements is tightly correlated to the amount of  $^{56}\text{Fe}$  that is present within the remnant. It was determined that approximately 50% of the total iron content within type Ia supernovae is represented by  $^{56}\text{Fe}$  (Nomoto et al. 1997). By investigating the ratios between this isotope and nickel, chromium and manganese, it is possible to envision a picture of the free neutron emission and distribution throughout Kepler at the time of the explosion. In turn, this neutron flux is generated by the density conditions within the progenitor white dwarf prior to its detonation.

Nickel is the first iron peak element to be synthesized. It is a byproduct of the silicon burning process that occurs in the terminal evolutionary stages of massive stars. Its subsequent release during the supernova explosion prompts a series of reactions that alter the composition of the material environment. The unstable nucleus of  $^{56}\text{Ni}$  undergoes beta decay and transitions toward  $^{56}\text{Co}$ , a short-lived particle that marks the closest local minimum in the iron peak diagram. Upon release of another beta particle, the  $^{56}\text{Co}$  isotope is converted into the stable  $^{56}\text{Fe}$ .

Chromium and manganese abundances are tightly intertwined. The only stable manganese isotope that accounts for its emission is  $^{55}\text{Mn}$ , a particle that requires low neutron capture timescales in order to be formed. The unstable  $^{53}\text{Mn}$  isotope, which boasts the highest half-life among the isotopes of this species, is converted into  $^{53}\text{Cr}$  through beta decay. Each of these  $^{53}\text{Mn}$  isotopes may either capture neutral particles and evolve into a stable nucleus, or transition into chromium. As a result, by comparing current abundances of manganese and chromium, it is possible to estimate the neutron flux generated by the type Ia explosion.

Stable forms of argon and potassium are also formed during various stages of the supernova explosion. Argon is a product of the radioactive decay of the  $^{40}\text{K}$  isotope, either by  $e^-$  emission or  $e^+$  absorption. In turn,  $^{39}\text{K}$  and  $^{41}\text{K}$ , the stable forms of potassium, are synthesized during the explosive oxygen burning stage that precedes the silicon burning. In a way similar to the distribution of nickel inside the volume, the supernova detonation is responsible with scattering the potassium atoms throughout the plasma

One last effect that can factor into the distribution of chemical species throughout the supernova remnant consists of the under- or over-ionization of the plasma in very young and in mature remnants, respectively (Vink 2011). In particular for recent type Ia supernovae, the pressure and temperature conditions within lead to longer ionization timescales than initially predicted by their computed physical parameters. As a result of the expansion of the material inside the remnant, the density inside might be sufficiently low that interactions between particles occur at a lower rate in comparison to what the observed temperature values might indicate. This phenomenon can be traced in most of the remnants of supernovae that have occurred within the past several hundred years and can account for the underproduction of important isotopes within the constituent plasma.

## 2.2 SN 1604 - Kepler's SNR

Kepler's supernova remnant has been the subject of extensive prior research that investigated a wide array of its defining characteristics, ranging from unravelling the object's origin (Bandiera 1987), up to the classification of minute subarcsecond structures that lie within its volume. Due to the large quantity of information readily available on the remnant, as well as a series of more recent high quality x-ray observations performed by XMM-Newton in 2001-2003 and Chandra in 2007, Kepler stands out as a suitable candidate for the investigation of iron peak element abundance.

Following its discovery in the early 17<sup>th</sup> century, SN 1604 has constituted a point of interest for astronomers and physicists alike. It remains one of the last recorded supernova explosions to have occurred within our galaxy, with a peak magnitude high enough for its signal to have been detectable on Earth by naked eye. In terms of position, it is situated at  $l = 4.5^\circ$  and  $b = 6.8^\circ$  on the night sky, with a diameter spanning across a distance greater than 200'' (Blair 2004). Nonetheless, its geometrical properties such as radius and shock velocity are largely unknown, mostly due to the lack of a precise distance measurement to the object. The specified coordinates place the remnant at a position  $6.8^\circ$  above the galactic plane, on the axis connecting our Sun to the center of the galaxy. The increased object density contained within the field of view brings forth difficulties in recording fine structures, as well as making an accurate determination of the distance parameter impossible. The crowded field of stars surrounding the remnant makes thin filaments very hard to detect and may lead to a confusion between optical knots within the volume and the emission of stars in the background (Bandiera 1991).

To this end, several constraints have been derived throughout the years, ranging from a minimum of 3 kpc and stretching up to 10 kpc. The currently adopted standard places Kepler's supernova remnant within a 4.8 - 6.4 kpc distance range (Reynoso & Goss 1999). Both the lower

and upper boundaries were derived from the object's relation with H1, in terms of either photon absorption or of the relation between the shock velocity and the proximity to the clouds. Regardless, the interval remains rather inaccurate and only serves to constrain the radius parameter between roughly 2.18 pc and 2.90 pc (Blair 2004).

The light emission can be characterized by a roughly spherical shell. A bright region to the north, stretching almost 100'' across, dominates both the optical and x-ray spectrum. Conversely, the object displays peculiar underdensities in the south, predominantly in the south-western region. Observations made in the optical range have identified two major components of emission. On the one hand, the collision between the strong radiative shocks has led to the formation of large mass knots that are recognizable throughout the entire volume of the supernova remnant. Furthermore, thin filaments are visible in the  $H^\alpha$  band. A mapping of these filaments across the spherical shell shows the most of their emission occurs at both 8.0 and 5.6  $\mu m$ , with most of these being dominated by the longer wavelength band (Blair et al. 2004, using data from the Spitzer Space Telescope).

The asymmetry seen in most wavebands remains one of the defining features of Kepler's SNR. In order to more properly address the multitude of knots and structures scattered throughout the entire volume of the object, a recent study has defined several regions of interest that are prominently visible in the x-ray waveband (Cassam-Chenai et al. 2004). In the interest of consistency, the same division and nomenclature shall be employed in the analysis at hand. The image below (Figure 1) marks the identified regions. The northern and southern rings are the structures resembling the arms of spiral galaxies, both enveloping the inner volume of the remnant. The western and eastern ear lie on a secondary axis of symmetry that is further enhanced by the crossing ring near the center. The bar, hand, shoulder and eyes are features that also appear bright in the x-ray spectrum.

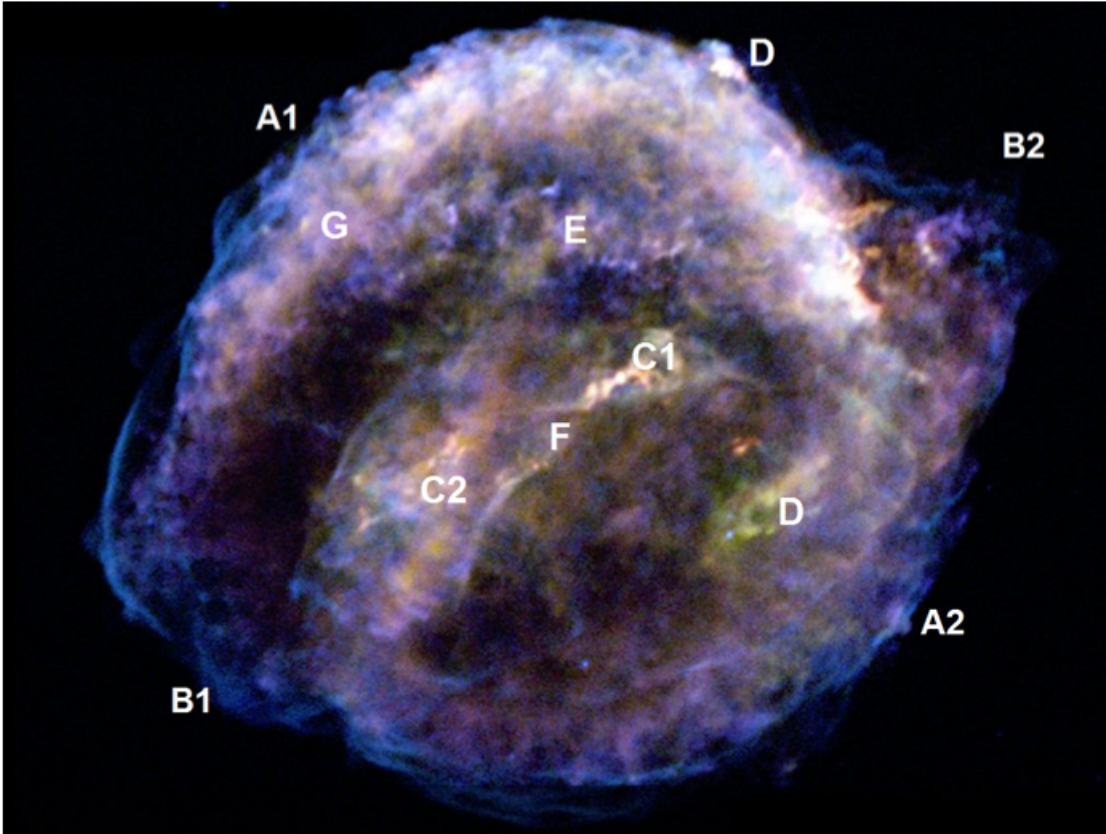


Figure 1: Three color image of Kepler's SNR, courtesy of the Chandra X-ray Observatory photo album. The white texts marks specific regions of interest throughout the object: (A1) northern ring, (A2) southern ring, (B1) eastern ear, (B2) western ear, (C1) western eye, (C2) eastern eye, (D) elbow, (E) bar, (F) crossing ring, (G) shoulder.

The same paper that defined this specific classification also employed it in an investigation of the peculiarities observed in Kepler's x-ray emission. By looking at a set of high quality observations taken by XMM-Newton in early 2001, the authors attempted to establish a connection between the behavior of the Fe and Si line complexes, the two most prominent components of the spectrum, and the apparent asymmetry of the volume. They looked at how the element profiles vary with increasing radius, as well as across the dominant features of the x-ray emission. Their conclusions were twofold. On the one hand, the contribution of Fe L and Si K is spread out comparably both to the north and towards the south, with only

the eastern ear showing a larger concentration of the former. Spectra of regions close to the outer edge of the remnant reveal that silicon protrudes up to larger radii than iron. By taking into account these facts, it is possible that Kepler displays an *onion layer* structure, with silicon overlapping iron in intertwining concentric shells. Furthermore, a distinction could be made between the contribution of the Fe L and Fe K lines across the entire volume. It was observed that Fe K was more prominent near the center of the remnant, with its contribution waning at larger radii, whereas Fe L was more evenly dispensed throughout the material composition. This observation provides some insight into the temperature distribution across

the volume, as well as the ionization timescale that characterizes the medium. The Fe K rich central region indicates higher temperatures that gradually decrease as we move toward the edges of the remnant. Theoretical models predict that the peak temperature is reached either at the contact discontinuity between the ejecta and shocked ambient medium, as is the case for type II core-collapse supernovae, or near the reverse shock traveling through the material, as predicted for type Ia candidates. The iron profiles shown indicate an affinity towards the second category. However, there were difficulties in fitting the simulated temperature gradient to the observed values, which prompts the existence of further interaction between the ejecta and the circumstellar medium.

Kepler is widely referred to as a type Ia supernova, whose progenitor was the white dwarf evolution of a population II star. Its structural similarity to other type Ia candidates, both in terms of its emission profile and chemical composition, project it as a definite candidate of this category. The possibility that the remnant has originated from the core-collapse event of a massive star, rather than the explosion of a white dwarf, was suggested throughout a series of past papers. However, with the advent of more advanced technology, less than two decades ago, it was possible to more accurately determine Kepler's structure and chemical composition. By analyzing the mechanisms that were involved in its evolution and by comparing it to other supernova remnants, it became widely accepted that the object belongs to the type Ia category.

Nonetheless, some details regarding the nature of the remnant remain uncertain. One of the main questions still standing is whether the supernova explosion originated from a single or from a double degenerate system, with heavy implication into the mechanisms that served as a driving force in Kepler's evolution. On the one hand, a single degenerate system is characterized by the accretion of material onto a white dwarf from a companion star, commonly a red giant. Throughout this process, the WD

gradually increases its mass. As it nears the Chandrasekhar limit of  $1.44 M_{\odot}$  the degeneracy pressure inside the star becomes insufficient to counteract the gravitational pressure, resulting in a supernova. A trademark of the single degenerate system, one that can be observed at later stages in the remnants, is the fact that traces of the companion star remain visible after the explosion and can be identified via x-ray close to the geometrical center of the object.

As its name suggests, a double degenerate system is made up of two white dwarfs drawn together in orbit by their gravitational pull following various collision processes. As the binary system loses angular momentum, the two stars come closer and closer together. The ensuing collision results in a super-Chandrasekhar mass white dwarf which in turn undergoes a supernova explosion. Throughout the past years, several attempts have been made to clearly identify traces of a progenitor or companion star within the remnant. Despite a series of high quality x-ray observations made both by XMM-Newton and Chandra, no evidence has been found that would point toward a single degenerate or double degenerate scenario regarding the origin of Kepler.

Its position with respect to the galactic plane is also indicative of a Type Ia origin. The relatively large distance between the remnant and the galactic plane favors the theory of a white dwarf evolved from a metal-poor population II star (Blair 2004). Nonetheless, upon studying the space motion of the object, it can be remarked that Kepler is rapidly shifting towards the northwest, with a velocity that exceeds the expectations corresponding to a Type Ia deflagration. Extensive observations have measured that the supernova remnant moves with a velocity of approximately  $0.03''$  per year (van den Bergh 1973). Although a precise determination of Kepler's space motion cannot be provided in lack of a proper distance measurement, the estimated velocity derived by using the 4.8 - 6.4 kpc range points towards a value within  $200 - 300 \text{ km s}^{-1}$ , in the direction of the northwestern bow shock. In turn, the object's tendency

to rapidly distance itself from the galactic center could have been explained by attributing its origin to that of a massive runaway star from a previous supernova (Blair 2004). Specifically in close binary systems, the explosion of one of the two members may lead to the expulsion of the other, with an imprinted velocity matching that of the observed remnant. The traveling star may evolve into a white dwarf and later into a supernova while retaining its space motion.

The asymmetry visible both in the optical and x-ray makes Kepler’s structure stand out among other type Ia supernova remnants. At such a high redshift, the density and overall consistency of the interstellar medium should not vary on a small scale, making it impossible to attribute the inhomogeneity of the object to variations in shock propagation due to the surrounding environment. The standout region is the dominant optical knot that lies in the northwestern section of the volume. By all accounts, its existence is related to the bow shock generated from the rapid space motion of the object. Due to the initial velocity of the star at the moment of the explosion, the matter found in the bow shock stagnates, whereas the one found diametrically opposite to it tends to get spread thinner. A lower limit for the formation of the observed bow shock was computed and a supersonic parameter value was determined as the needed threshold (Bandiera 1987). With a supersonic speed of roughly 250 km/s away from the galactic plane, Kepler’s SNR exceeds this limit regardless of the relative inaccuracy of its distance determination. This phenomenon carries sufficient weight to account for the northeast - southwest asymmetry of the remnant.

Although the effects of the stellar wind accreted in the progenitor phase are not strong enough to account for the remaining inhomogeneity across the entire remnant, they do influence the composition of the bright northern region to great extent. In doing so, they provide an important contribution toward understanding the origin of the supernova. It was observed

that the overdensity exhibits a higher concentration of nitrogen among an otherwise solar metallicity. A recent study made a connection between these abundances and the evolution of Kepler’s circumstellar medium, with strong evidence towards a single degenerate progenitor model (Chiotellis et al. 2011).

Stellar evolution theory dictates that a star on the asymptotic giant branch can enrich their surface composition with nitrogen if their masses exceed  $4M_{\odot}$ , while keeping its other material constituents at solar quantities. By having such a candidate as the donor star of a single degenerate system, it is possible to create a circumstellar medium similar to what is observed in the actual remnant. The study predicted that, in the case of a  $4 - 5M_{\odot}$  AGB, the slow stellar wind could accrete onto the white dwarf, whereas surface nitrogen would accumulate into a surrounding shell. The upcoming explosion mechanism, coupled with the evolution of the remnant material as a result of its space motion away from the galactic plane, would lead to the formation of the peculiar northern region. This claim is strongly supported by measurements of element concentrations therein. Not only would the AGB donor theory provide a reasoning behind the overabundance of nitrogen in that specific region, it would also explain why the other chemical compounds amount to an approximate solar metallicity.

Ongoing investigations into the nature of Kepler’s supernova are still attempting to find irrefutable evidence regarding the nature and evolution of the remnant. Recent advances in technology have led to better observations and more accurate measurements being made, making it possible to delve even deeper into the pool of information contained within the object. This study itself will attempt to use parts of this knowledge in order to provide a contribution to the field of research and to bring the issue one small step closer to its final solution.

### 2.3 The Datasets

The launch of a new generation of space telescopes has heralded a new era for x-ray observations. Due to the high levels of absorption generated by the Earth’s atmosphere, it is difficult to record the emission of hot material in the Universe from the surface of the planet. With the advent of NASA’s Chandra X-ray Observatory, as well as ESA’s X-ray Multi-mirror Mission (XMM-Newton), it is now possible to properly detect and study thermal sources that were inaccessible prior to these efforts.

For the purpose of this paper, two sets of x-ray data have been processed and analyzed. The first was collected from Chandra’s online database and consists of a merged file of six different observations taken between the months of May and July 2006. The Advanced CCD Imaging Spectrometer aboard the space observatory enables the detection of incoming x-rays while also measuring the energy of each incoming detection. This technology allows for the filtering of various signal ranges and for isolating the emission of specific elements within the derived spectral profiles. The high resolution spectra make this dataset ideal for most of the analysis performed here. The high number of projected counts that the CCD records within the 0.5 - 6 keV allows for a good analysis of the iron, silicon, sulfur and calcium line complexes, while also making it possible to track variations

in the less pronounced argon and chromium lines. Above the 6 keV threshold, the observed number of counts decreases. This complicates the filtering of manganese and nickel lines from the continuum emission, as well as making it difficult to obtain a proper fit of the Fe K line complex, situated in the 6.1 - 6.4 keV range.

The second dataset was employed with the intention of confirming the findings enabled by the Chandra observations, as well as enabling a better sampling of the high energy continuum. The high quality images of Kepler’s SNR taken by XMM-Newton in March 2001, were taken with the European Photon Imaging Camera (EPIC) instrument aboard the observatory. The latter is composed of two separate CCD arrays. The Metal Oxide Semi-conductor (MOS) is an array of seven CCDs separated into two nodes which are capable of registering incident pixels of up to 15 keV with high precision. The pn camera array, the second module built into EPIC, is used for capturing uniform across the entire field of view, as a result of its monolithic fabrication with no dead space between adjacent CCDs. Overall, the instrument boasts a wider field of view and energy range, at the cost of a slightly moderate resolution. As such, the XMM-Newton information is used solely as a secondary dataset, in order to more accurately verify the profiles of the high energy emission lines.

	Chandra	XMM-Newton
Instrument	ACIS	MOS1
Exposure time [ $10^4$ s]	15.7	3.07
Net count rate [cts/s]	4.028	2.276

Table 1: Basic observation parameters of the two datasets employed in the analysis.

### 3 Data Analysis

The data collected from the Chandra Observatory's data archive was compiled into a single event file and processed with the help of the Chandra Interactive Analysis of Observations (CIAO) software. The input and output .fits files were displayed on the SAO Image DS9 and fv FITS Viewer graphical programs. The spectral analysis and fitting was done using the XSPEC package recommended by the Chandra website, as well as the SPEX data analysis tool developed by the Netherlands Institute for Space Research. All of the procedures were run on a Macbook Pro platform, powered by an Intel Core 2 Duo processor operating at a speed of 2.4 GHz, with a RAM capacity of 4GB. The device featured the Mac OS X 10.6.8 Snow Leopard operating system, which could accommodate and handle all of the required software packages.

The initial steps of the analysis sought to identify key regions and peculiarities in the observed x-ray emission throughout the supernova remnant. A top-down decomposition was chosen, as a more efficient way of advancing the investigation and managing the collected data. By starting out with the full spectrum analysis, covering the entire 200" diameter, it was possible to derive a general overview of the element composition within the object and compare this to other known supernovae of the same category. Furthermore, by comparing and contrasting this information, a strong baseline could be inferred that served as the starting point for the upcoming more detailed analysis. In addition, it allowed for a rough calibration of the fitting package with regards to the plasma components defined in the model.

The regions highlighted in Figure 1 were the next to be investigated. Their peculiar distribution throughout the volume of the remnant could point in the direction of local over- or underdensities that might be correlated to the concentration of iron peak elements. This analysis seeks to correlate elements in the visible structure of Kepler's SNR to its chemical com-

position, to the extent at which the observations permit.

The subsequent phase of the analysis involved the use of principal component analysis in order to reveal correlations between the various element species within the volume. This procedure highlights those components within a high dimensional data set that provide the maximum variation and uses those to construct an orthogonal system, with the directions of the axes given by the components themselves. In doing so, it will be possible to identify the regions with the most visible contributors to the abundance distribution throughout the remnant.

#### 3.1 Full Spectrum Analysis

From a broader perspective, Kepler's structure and chemical composition resembles that of other type Ia supernova remnants whose explosions are dated back to the 16th century. The roughly spherical distribution of its material constituents throughout the ISM, as well as a certain degree of homogeneity when compared to core collapse supernovae, are clear indications of the white dwarf nature of its progenitor.

Nonetheless, there are notable differences between SN1604 and its type Ia peers that become noticeable at a closer inspection of their physical and chemical parameters. Despite their analogous origins, which account for the majority of their similarities, there are other distinguishing factors that could have affected their development and could have led to the disparities observed today. Different properties of either their progenitor stars, their donor companions or of the overall interstellar medium can lead to diverging natures of type Ia supernovae. Moreover, external events that have occurred in the past centuries are also plausible candidates for altering the characteristics of the remnants. Valuable insight into the nature of these objects can be derived from the analysis of these discrepancies and from deducing how those came to be.

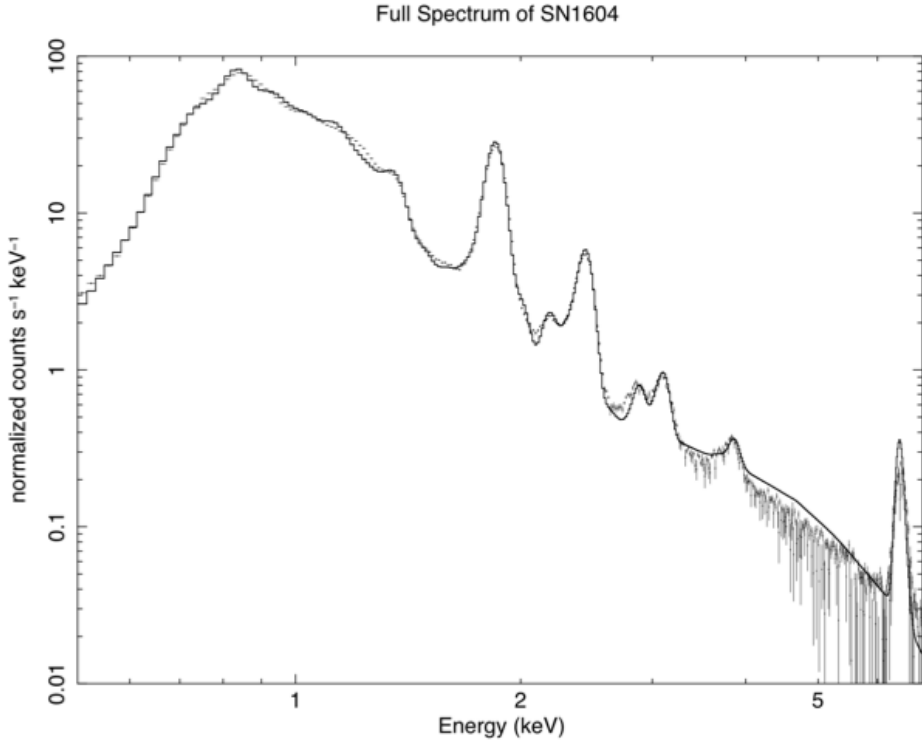


Figure 2: A two component non-equilibrium ionization model fit onto the full spectrum of Kepler’s SNR. The most prominent contributors to the emission are labeled onto the graph.

Figure 2 shows the complete processed spectrum. In order to minimize the effects of foreign nearby sources and to provide a constant threshold for the emission in the surrounding environment, three background regions were selected from the observation. These lie at roughly  $40''$  above the northern overdensity of the remnant and measure less than  $20''$  in diameter. The background emission spectrum is included as a guideline in the appendix. The model fitted onto the spectrum uses a two component plasma model that accounts for the non-equilibrium ionization that is characteristic of all young type Ia supernova remnants. It is composed of the multiplicative Tuebingen-Boulder ISM absorption model (tbabs) and two additive non-equilibrium ionization collisional plasma models (vnei).

The **tbabs** model was designed to make better use of the physics of the interstellar medium when determining the average cross sections of the dust particles and molecules that lead to photoionization processes (Wilms et al. 2000). These new emissions can alter the spectrum of the observed object significantly and must be accounted for in the data processing. The authors break down the effects of the ISM into three categories, which they have named phases. The contributions of the gas, molecule and grain phases are individually detailed, ultimately leading to a better prediction of the photoionization. The improvements this model brings to the proper determination and calibration of x-ray spectra are especially important for datasets taken with high-resolution instruments. As such, it was selected as a proper anal-

ysis tool for Chandra’s observation of Kepler’s SNR.

The two **vnei** models account for the shocked ambient medium and for the shocked ejecta component, both with different underlying physical parameters. The timescale required to reach ionization equilibrium is larger than its current age, given that SN1604 is a relatively young remnant. In addition, the collisions that trigger the ionization process throughout the mass of the object occur at a relatively low rate, due to the physical constraints, leading to an overall underionization effect (Vink 2011).

Nonetheless, while they do follow the same general guideline described above, the two plasma components are quite different in nature. The parameter that best sets the two apart is the plasma temperature in each of the components. The shocked ejecta is considered to be hotter than the shocked ambient medium, leading to different element composition and abundances being produced as a result of ionization. The vnei model requires the input of a single, constant temperature for each of the components, as well as abundances for the following elements: He, C, N, O, Ne, Mg, Si, S, Ar, Ca, Fe and Ni.

Parameter	First <i>vnei</i> component	Second <i>vnei</i> component
Plasma temperature (keV)	2.09	5.25
Ne	4.20	frozen
Mg	0.31	frozen
Si	frozen	3.58
S	frozen	3.66
Ar	frozen	2.74
Ca	frozen	3.03
Fe	23.67	2.04
Ni	frozen	frozen

Table 2: Best fit parameters for the tbabs model with two non-equilibrium ionization components. The element contribution values are expressed in units of solar abundance. The second column shows values for the shocked ambient medium, whereas the third column holds those for the shocked ejecta.

The results provided by the best fitting model are presented in table 2. The first *vnei* component was chosen as the shocked ambient medium. The lower plasma temperature (roughly  $T_{am} = 2keV$  as predicted by the model) is responsible for the iron L-shell emission features that are so prominent in the complete x-ray spectrum. In addition, this component accounts for the emission of elements such as oxygen, neon and magnesium (Behar 2008). Although a certain contribution to the silicon line complex comes from the shocked ambient medium, its impact on the shape of the overall spectrum is negligible when compared to that of the shocked ejecta. For this reason, the Si

abundance in the first component was not denoted as a free parameter and kept at a fixed solar value instead.

The hotter plasma component represents the shocked ejecta material. With temperatures more than twice as high as those of the shocked ambient medium ( $T_e = 5.2 keV$ ), this material predominantly accounts for the emission lines above the 1.8 keV threshold. The prominent silicon and sulfur contributions, those of argon, calcium and nickel, as well as the Fe K line complex, require higher ionization rates that are facilitated by the increased collision rate inside the shocked ejecta.

Although the analysis tool permitted the use of nickel abundance as a free model parameter, the profile of the spectrum at the far end of the high-energy continuum dictated against it. Despite the very good resolution of the Chandra observations, which have led to a good fit in the range  $0.5 - 7 \text{ keV}$  range, the net count rate at higher energies is lower than the accepted limit. Although it is possible to determine a model profile that roughly fits the estimated nickel emission within 7 to 8  $\text{keV}$ , the resulting lack of physical significance swayed the decision in favor of freezing Ni abundances to solar values. A more detailed analysis of the high-energy continuum will be performed in section 3.4 using the dataset provided by the XMM-Newton observatory. Therein, the shape and prominence of the Ni emission line complex will be more thoroughly discussed.

Chromium and manganese could not be set as free model parameters during the fitting of the model. Moreover, the particular nature of their synthesis process gives them a more local character which is not appealing when discussing the complete spectrum of the remnant. Their abundances will be derived and specified for each of the regions investigated in section 3.2 in an attempt to correlate them to the more pronounced feature of the x-ray spectrum, such as the Fe L, Fe K and Si lines.

Additional information can be derived from the comparison of Kepler's spectrum to that of other type Ia supernova remnants. Figure 3 displays two images sampled with Chandra's ACIS tool. One belongs to the well-documented SN1572, Tycho's SNR, and the other to SNR 0519-69.0, a younger type Ia detected in the Large Magellanic Cloud.

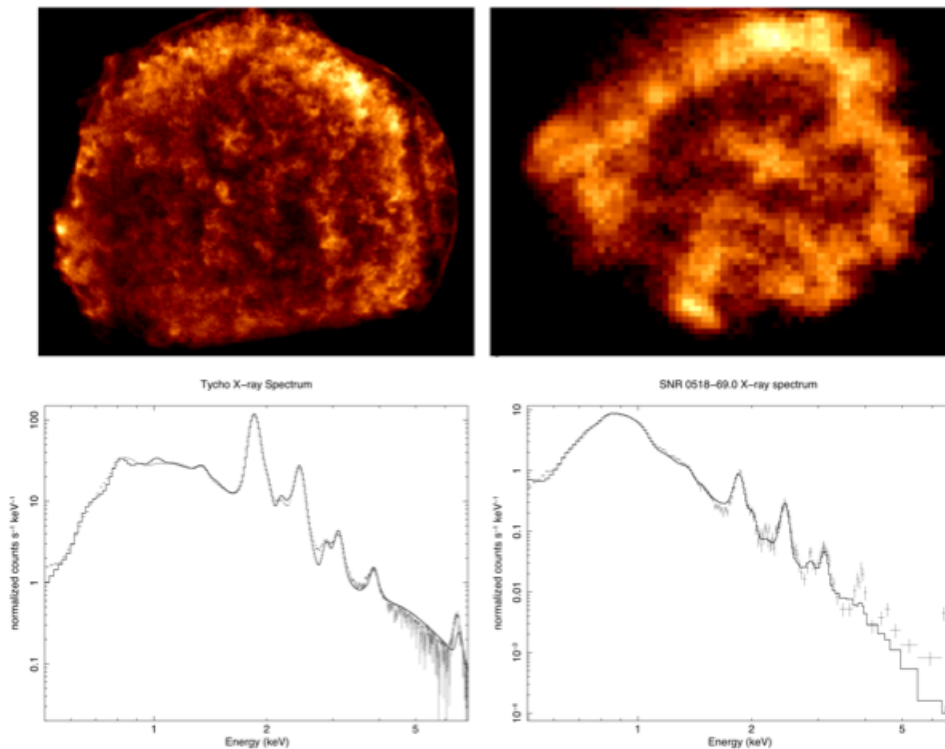


Figure 3: Fitted spectra for two type Ia remnants: Tycho's SNR (left) and SNR 0519-69.0 (right).

**Tycho** was chosen as a benchmark due to both the extensive information background provided by previous studies, as well as its overall similarity to Kepler. Currently, Tycho is one of the only two confidently known type Ias in our galaxy, alongside SN1006. Both it and Kepler are remnants within the Milky Way whose supernova explosions were observed at the end of the 16th century, within the rough span of 32 years. The occurrence of two type Ia supernovae visible with the naked eye within such a narrow timeframe and in relative proximity to the Earth should be considered a sign of good fortune. Their evolutions can be investigated in parallel to one another, with any contrasting differences providing insight into the peculiarities that characterize each of the remnants.

A brief look at their emission spectra in the x-ray band already reveals a striking discrepancy. The Fe L / Fe K line ratio is much lower in the case of Tycho's SNR with a reduced contribution of the iron L-shell emission. We have previously identified Fe L to be one of the main constituents of the shocked ambient medium material that accounted for the lower temperature plasma within the object.

Although the silicon and sulfur profiles match those we have seen in Kepler, the relative abundances of argon and calcium modeled for Tycho, measured as ratios of Fe K, exceed their corresponding values. The increased presence of these atomic species can be attributed to any of two physical factors. On the one hand, the three decades of evolution that Tycho has ahead of Kepler have allowed for more collisions and interactions to occur, which is indicative of a higher ionization degree. Although it can only be indirectly inferred, it is possible that abundances of other elements found above the high energy continuum follow the same pattern. This dictates that chromium and manganese concentrations are also expected to be lower in Kepler.

Another possible reasoning behind the differences in x-ray emission, one that also encompasses the disparity of the Fe L line complex,

refers to the temperature difference behind the two plasma components of each remnant. The thermal ratio between the shocked ejecta component and the corresponding ambient medium predicted by the model fitted to Kepler's spectrum indicated a value of 2.5. Conversely, in Tycho, that ratio is approximately 3. Although the individual values computed by the models indicate overall higher values for Kepler's plasma, the higher ratio between the two components in Tycho may account for the greater prevalence of Si, S and heavier atomic species at the expense of Fe L.

SNR **0519-69.0** was recently identified as the remnant of a type Ia supernova, virtue of a series of high quality Chandra and Hubble observations. Although it is positioned outside of our galaxy, at more than 50 kpc, inside the Large Magellanic Cloud, its relative young age make it an interesting term of comparison to Kepler. In terms of their x-ray emission, the distribution of material inside the remnant is remarkably similar in both Kepler and 0519. A comparable 'spiral limb' structure, complete with the very bright northern region, indicates that the two remnants have had an analogous evolution in terms of configuration. A look at the two spectra confirms that this similarity extends to the level of their chemical composition as well.

The total number of detector counts is much lower in case of the 0519 dataset when compared to the much better quality images of Kepler and Tycho. This reduced number of data points above the 4 keV threshold makes it difficult to fit a proper model over the high energy continuum region. Thus, there is little relevance in terms of physical significance when comparing the iron K-shell emission of the two remnants. However, the line profiles found closer to the low energy boundary of the x-ray spectrum are well defined and fit within a reasonable confidence range  $\chi^2 < 3$ . Unlike in Tycho's emission spectrum, 0519 displays the same prominent contribution of the Fe L line complex provided by the low temperature plasma component. In addition, the Si and S profiles that are characteristic of a young supernova remnant

are also visible here, although their contribution now rivals that of Ar and Ca. The latter two elements have a considerably lower contribution to the overall spectrum in Kepler, with a recorded count rate / s keV approximately twice as high as the average level of the continuum. In SNR 0519, the line complexes of both argon and calcium are comparable to those of silicon and sulfur, indicating higher levels of ionization inside the shocked ejecta material. This is indicative of more favorable ionization conditions than in Kepler, either by means of a higher plasma/electron density or of a richer neutron excess induced in the early stages of the supernova explosion.

The structural similarity seen between Kepler and 0519 is doubly more interesting considering the difference in overall size between the two objects. Remnants in the Large Magellanic Cloud need to be significantly larger in diameter in order for them to be detected and properly observed, due to the greater distance when compared to those in our galaxy. SNR 0519 makes no exception. It is approximately 7 pc wide (Edwards 2012), almost twice as expanded as the Kepler remnant. Despite this discrepancy, there are many common regions that can be identified within the two SNR. Aside from the prominent overdensity near the top, the Chandra x-ray observations reveal the existence of bright northern and southern rings, as well as a central crossing ring. This is indicative of analogous physical conditions and processes that have affected the evolution of the two objects and that functioned on two distinct scales. Asymmetries in the ejection velocity of the material, as well as in the surrounding interstellar medium, are intrinsic properties to each supernova explosion due to their random nature. As such, they cannot be used to draw a parallel in the analysis aside from explaining a coincidental distribution of the gas and dust deformations.

The outer edges of Kepler and 0519 are circular in nature and the distribution of any protruding regions, such as the ears shown in Figure 1, shows no correlation with the asymmetries

inside the volume. As it was concluded for SN 0519, there appear to be no methodical deformations that would affect specific sectors of the remnants (Edwards 2012). As with Kepler, the bright northern region that is highlighted by the x-ray filter can be attributed to an overdensity of accumulated material. To the extent of our knowledge, this is due to the space motion of both objects. The fact that both of the overdensities are found in similar areas of the remnants is indicative of a parallel alignment of their velocity vectors.

Analysis of Kepler’s complete x-ray spectrum can still provide additional insight into the nature of the remnant and its evolution. By investigating the line strengths of the main emission contributors, it is possible to derive information regarding the temperature profile across the object’s volume, as well as to infer the relative position of the reverse shock that propagates towards the center of the remnant.

One indication of the temperature distribution inside the SNR material is given by the ratio of the L- and K- shell iron line emission. As previously mentioned, the former is one of the main constituents of the cooler shocked ambient medium component, whereas the latter is synthesized by beta decay processes inside the hotter shocked ejecta. By looking at their relative strengths across the volume, as well as how early they peak as a function of radius, it is possible to determine a rough temperature gradient and project it onto the remnant itself.

The method chosen here was to split the object into ten concentric circles, starting from a central circle of radius  $10'' \pm 1''$ . Nine annuli were overlapped onto the image, with an increment of  $10''$  for the major radii of each subsequent figure. Thus, the final annulus had a major radius of  $100''$  and encompassed the remnant entirely. Individual spectra were generated for each of the ten regions and from them the line complex strengths of Fe L and Fe K were determined. Due to specific effects that may influence the shape of the spectral features, such as shifts in line position and

peaks, it was unadvisable to use the height of each emission line on the analysis. Instead, the equivalent width was chosen as a measure due to it being unaffected by spectral shifts. This parameter is determined as the width of a rectangle that has a height equal to the continuum emission and a surface area equal to that of the corresponding line profile. It is given by

$$W = \int \frac{F_c - F_E}{F_c} dE$$

where  $F_c$  is the continuum level,  $F_E$  is the level of the line profile and  $dE$  is the sampling, in

units of energy (Sarazin 2008). A visual representation of how the height of a spectral line can be converted to its equivalent width can be seen in Figure 4. Some effects that alter the line profile can leave the total flux, measured as the area below the line, unaltered. One such example is the Doppler broadening effect that shifts photons to both higher and lower energies away from the peak, due to the individual motion of particles inside the material. This factor would consistently alter the position of the peak and flatten the overall profile, but would leave the measure of the equivalent width intact.

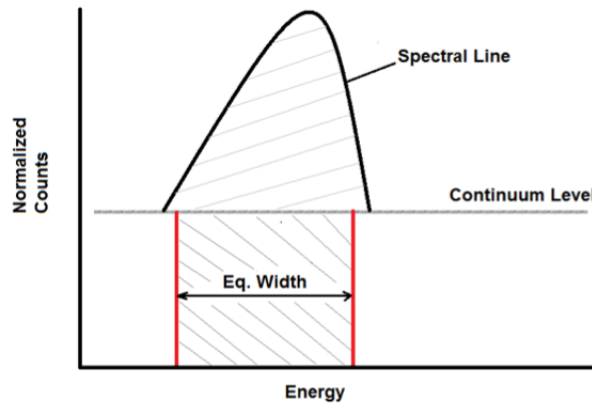


Figure 4: The equivalent width of an emission line. The height of the rectangle coincides with the continuum emission. The hashed areas below and above the continuum are of equal measure.

The SPEX analysis tool can provide a measure of the equivalent width corresponding to the spectral line profiles defined by the fitted model. It requires the input of an additive model for which the integrated photon flux is determined. In order to single out the emission of the Fe L and Fe K components, the two existing line profiles were fitted with an additional gaussian across their respective energy bands. The range of the energy levels used, along with the associated errors, were taken from the National Institute of Standard and Technology (NIST) database. Despite its overall convolution, the broad L-shell iron line complex is predominantly comprised of Fe XX species

that span from 0.86 to 1.34 keV. To account for the presence of other iron atoms and ions, the total range for fitting the Fe L gaussian was selected as 0.72 - 1.43 keV. At the far end of the spectrum, the Fe K line complex proved easier to untangle. Above the 6 keV threshold, Fe XXV accounts for most of the iron emission. As such, the fitted range for the second gaussian coincides with the presence of Fe XXV within 6.30 - 6.65 keV.

A temperature gradient for the plasma inside the remnant can be derived by comparing the ratios of the Fe spectral lines within each of the ten sections. Table 3 shows the evolution

of this ratio across the radial profile. It should be noted that individual values for the equivalent widths were not included due to the fact that variations in the total count rate across different regions make it futile to attempt direct comparisons of line strengths. For instance, the two annuluses that correspond to 0.8 - 0.9 R and 0.9 - 1 R traverse the bright over-density found in the north of the remnant. Thus, the total number of recorded photons is greatly enhanced relative to the more central regions. While this also affects the shape of the continuum, the effect mostly impacts those energies where there is already a high detection rate throughout the remnant. An implied normalization effect is obtained by the division of one line strength to the other, thus canceling out the differences induced by disparities in the net count rate.

The distribution of the line strength along the remnant's radius is presented in Table 3. Although the discretization is coarse, with only ten individual regions marking separate steps in the gradient, it is possible to derive a rough estimation of the position of the hottest material component. The nature of type Ia supernova remnants dictates that the temperature distribution throughout the material is closely linked to the position of the reverse shock traveling back towards the center of the object. Unlike core collapse supernovae, where the plasma grows cooler with increasing radius, here the material becomes hotter the closer it is to the reverse shock. It is implied that the central and peripheral regions of the remnant are relatively cool, with a peak temperature to be found at a fraction inside the volume of the object.

Radial Increment	Fe L / Fe K
0 – 0.1 R	5.86
0.1 – 0.2 R	4.69
0.2 – 0.3 R	3.46
0.3 – 0.4 R	2.41
0.4 – 0.5 R	1.93
0.5 – 0.6 R	1.94
0.6 – 0.7 R	1.97
0.7 – 0.8 R	2.46
0.8 – 0.9 R	2.51
0.9 – 1.0 R	1.85

Table 3: Computed ratio of L-shell and K-shell iron inside ten distinct regions across Kepler's radius, as an indication of the temperature gradient. Higher values are associated with cooler plasma. Lower values correspond to hotter plasma.

The regions closest to the geometric center display the highest Fe L / Fe K quotient, in accordance to the theoretical predictions. A steep gradient spans across the 0 – 0.4 R range, indicating a sharp increase in temperature as we distance ourselves from the central area. At 0.4 R the variations between neighboring increments becomes very low, with values pertaining to each other's confidence range. This sudden decline in the slope of the gradient makes it

difficult to isolate the negative peak of the iron line ratio. The analysis indicates that the region contained within 0.4 – 0.5 R corresponds to the lowest value of Fe L / Fe K and is the most likely position of the reverse shock, although the narrow margin of separation between it and the 0.5 – 0.6 R region casts some doubt onto the matter. Figure 11, included in the appendix, serves as a visual representation of the computed temperature gradient.

### 3.2 Regions of Interest

The distribution of knots, filaments and overdensities across Kepler’s volume are mainly accounted for by the irregular nature of the remnant’s evolution parameters. Asymmetries in the surrounding interstellar medium, as well as in the initial propagation velocity of the ejecta material, have led to the formation of peculiar regions that are evidenced in the x-ray band. This section will focus on the emission spectra of the most prominent of those regions, as labeled in Figure 1, in an attempt to correlate their existence and position within the object with their chemical composition. In doing so, it will be possible to take a better look at the contributions brought by less abundant species, such as chromium and manganese, and map their relative distribution throughout the remnant.

The overall shape of Kepler’s supernova remnant features several axes of symmetry, delimited by pairs of bright x-ray regions on each end and intersecting the crossing ring (denoted as F in the figure) near the center. One such feature is marked by the presence of the two *rings*, one to the north of the object (labeled A1) and one to the south (A2). They constrain the ejecta material to a somewhat spherically symmetric spread, a specific trait of type Ia supernovae that tells their remnants apart from those of core-collapse explosions. The even distribution across these regions at diametrically opposite areas of the object might indicate a more homogeneous interstellar medium across this particular axis, with few distinctions at the level of their elemental abundances. Moreover, the position of the *rings* at the edges of the remnant favors the presence of synchrotron radiation that would affect the shape of the high energy continuum in the emission spectrum.

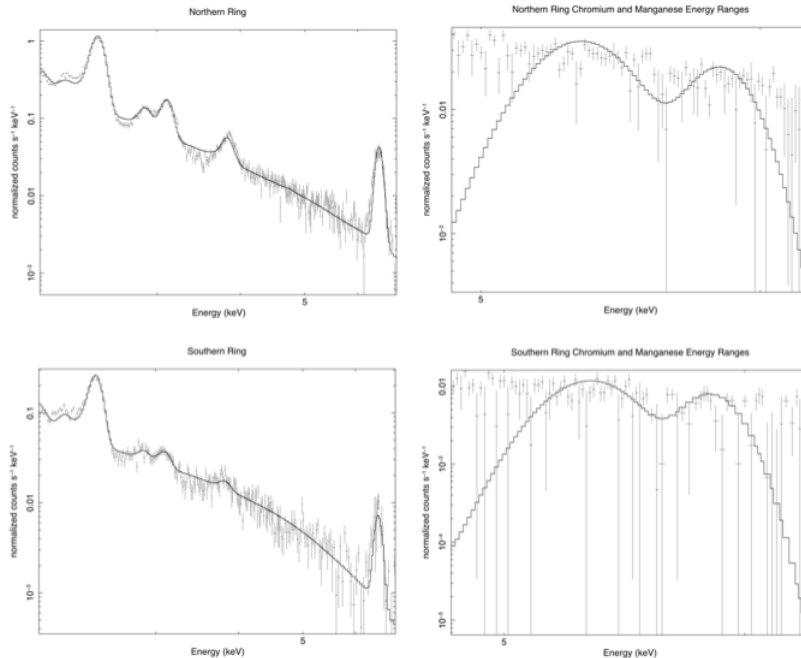


Figure 5: Emission spectra of the northern and southern rings. The images focus on the high energy continuum (left) and the specific ranges of the chromium and manganese emission (right).

The representation of the emission spectra above the 2 keV threshold outlines a series of notable differences in the chemical composition of the two regions. Although the emphasis here lies on the detection of less pronounced line complexes, the sulfur lines at 2.5 and 2.9 keV were included in the sample in order to obtain a better fit of the two component *vnei* model across the high energy continuum. An initial look over the overall profile of the spectrum indicates a higher contribution of heavier elements in the case of the *northern ring* that contrasts with the much smoother continuum of the southern region. The calcium line, in particular, is revealed to be even stronger than the one determined in the full spectrum model (Figure 2) with a predicted abundance 14.3 times that of its solar abundance. The strength of the argon line is also comparable, at 7.3 times its solar abundance.

Although there is a considerable difference in

the computed profiles of argon and calcium, both the sulfur and K-shell iron emissions are similar when comparing the two regions. Moreover their abundance values roughly match those determined in the analysis of Kepler’s complete spectrum. This implies that the shocked ejecta material present inside the *northern ring* favored the synthesis of argon and calcium throughout the evolution of its chemical composition, perhaps as a result of an asymmetric release of the free neutrons resulted from the supernova explosion. This phenomenon could have affected manganese abundances in a similar way, due to the element being highly sensitive to neutron excesses. Table 4 shows the best fit abundances for the three elements investigated. Due to the fact that the Fe L line complex was omitted from the sample, the plasma temperatures inside the model’s two plasma components were manually calibrated to values resembling those in Table 2.

Parameter	Northern Ring	Southern Ring
S	3.71	3.24
Ar	7.31	2.16
Ca	14.29	8.37

Table 4: Best fit parameters for the abundances of sulfur, argon and calcium that correspond to the model in Figure 5. The values are expressed in units of solar abundance. Their emission is part of the shocked ejecta material, whose plasma temperature was set at a constant value of 5 keV.

One factor that explains the continuum profile across the *southern ring* is the presence of synchrotron radiation at the outer edges of the region. Its influence on the x-ray emission spectrum is mostly felt above the 3 keV range where it affects the shape of the high energy continuum to the extent at which the latter could be fitted rather well by the addition of a power-law model. Although the Fe K line present at 6.5 keV is strong enough to disrupt the fit, evidence of an important contribution from the shocked ejecta material at lower radii inside the *southern ring*, it is undeniable that the re-

gion is also affected by synchrotron emission. Due to the greater density of material amassed in the topmost region, the contribution of the shocked plasma components outweighs that of synchrotron radiation, leading to the more pronounced line profiles determined for the *northern ring*.

As mentioned in the theoretical background section, the abundances of chromium and manganese as a good indication of the free neutron flux released during the supernova explosion. On the one hand, the synthesis of stable man-

ganeses isotopes is closely linked to the amount of neutrons present in the surrounding medium, due to the rapid nature of the beta decay processes involved. Conversely, chromium production is largely independent of the free neutron density. As a result, weighting these two elements one to another can provide a reasonable estimate of the initial neutron flux. The emission of both chromium and manganese within this specific x-ray band is constrained to the 4.83 - 6.10 keV energy range. Figure 5 (right) depicts two gaussian components fitted to the spectrum sample of both of the *ring* regions, with each profile corresponding to one of the two investigated elements. Using the transition energies listed in the NIST database, the emission range of chromium was estimated within 5.20 - 5.50 keV, peaking at 5.35 keV. Similarly, the manganese line profile was estimated within 5.75 - 5.95 keV, with a peak value at 5.85 keV.

In order to determine a measure of their line strengths, the photon flux corresponding to each gaussian was computed, along with the errors induced by continuum uncertainties. Due

to the similar electronic structures of the two elements, it is possible to use the line flux ratios in order to directly determine an estimate of their mass ratios by means of the following expression (Badenes 2010):

$$\frac{M_{Mn}}{M_{Cr}} = \frac{A_{Mn}}{A_{Cr}} \cdot \frac{F_{Mn}}{F_{Cr}} \cdot \frac{E_{Mn}}{E_{Cr}}$$

where  $\frac{A_{Mn}}{A_{Cr}} = 1.057$  is the ratio of their atomic masses,  $\frac{F_{Mn}}{F_{Cr}}$  is the photon flux ratio and  $\frac{E_{Mn}}{E_{Cr}}$  represents the ratio of specific emissivities per ion. A value for the latter parameter was also derived by Badenes, by means of interpolating along the atomic number sequence using data from the ATOMDB database. Although the analysis was directed towards the Tycho's SNR, it is applicable to young type Ia supernova remnant as a whole. Thus, the resulting value for the emissivity ratio was determined as  $\frac{E_{Mn}}{E_{Cr}} = 0.69 \pm 0.32$ . The photon flux is associated with the area between the spectral line profile and the continuum line, which can be computed using the SPEX toolset. The computed values are listed in Table 5 below.

Parameter	Northern Ring	Southern Ring
Chromium line flux [ $10^{-4}$ ergs/cm <sup>2</sup> /s]	$8.53 \pm 0.32$	$4.28 \pm 0.29$
Manganese line flux [ $10^{-4}$ ergs/cm <sup>2</sup> /s]	$5.86 \pm 0.36$	$2.89 \pm 0.40$
$\frac{F_{Mn}}{F_{Cr}}$	$0.69 \pm 0.29$	$0.68 \pm 0.27$
$\frac{M_{Mn}}{M_{Cr}}$	$1.05 \pm 0.57$	$1.04 \pm 0.53$

Table 5: Photon flux values computed for the gaussian fits corresponding to the chromium and manganese spectral line complexes in the northern and southern *ring* region pair. The mass ratio of the two elements was estimated by means of the method employed in Badenes 2010.

As predicted, the flux intensities for the chromium - manganese element pair were considerably higher throughout the *northern ring*, due to the fact that a large segment of the investigated region coincided with the x-ray bright plasma overdensity. Nonetheless, both of the ratios determined were of similar values,

within their respective error ranges. Further ensuing from Badenes' analysis is a direct relation between the Mn to Cr mass ratios and the fundamental properties of the progenitor star of a type Ia supernova. Using a variety of explosion mechanisms, the authors have attempted to establish a correlation between the free neutron

imbalance and the metallicity of the progenitor itself. Despite the different models involved (deflagration, delayed detonation), it was observed that a tight relation between the two parameters holds outside of the inner  $0.2M_{\odot}$  material. The correlation between the neutron excess, as predicted by the mass ratio between chromium and manganese, is correlated to the progenitor metallicity with a factor of  $z = 0.9972$  via the following power-law (Badenes 2010).

$$\frac{M_{Mn}}{M_{Cr}} = 5.3 \cdot Z^{0.65}$$

Using the values computed for Kepler’s northern and southern *rings* we find that the two regions predict a metallicity of  $0.083^{+0.078}_{-0.056}$  and  $0.081^{+0.071}_{-0.054}$  respectively. Although the uncertainties are large, the analysis predicts a supersolar metallicity for Kepler’s progenitor. In line with this result, the initial investigation performed on Tycho also projected a solar or supersolar metallicity ( $Z = 0.048^{+0.051}_{-0.036}$ ). By these indications, the two supernovae have more in common besides the close time interval between their explosions. Given the computed metallicities, the progenitors of the two remnants could also belong to the same population of stars.

The second axis, stretching from northeast to

southwest, is constrained by the two *ears* (B1 and B2 in Figure 1). The symmetry here is enhanced by the presence of the two *rings* discussed in the previous paragraphs, which border each of the two bisected halves. Nonetheless, these regions represent some of the most irregular features in the remnant, due to the fact that they break the spherically homogeneous distribution of the material. While the two can be regarded as separate instances of asymmetry in the ejection velocity at the time of the supernova explosion, their position at diametrically opposite ends might link their occurrence to one specific physical phenomenon. Instead of discussing the *ears* individually, as areas where the material has travelled farther away from the geometric center, the two have been coupled based on their position relative to one another. This analysis will attempt to discover whether the two were created as isolated events or rather as the outcome of a single large scale process. It is possible that the two *ears* are the protruding sections of a ring of material that has been ejected on a plane orthogonal to the one in Figure 1, at an angle of approximately  $40^{\circ}$  and approaching the plane of the observer. In this instance, it is expected that the chemical compositions of the two *ears* exhibit a larger degree of correlation.

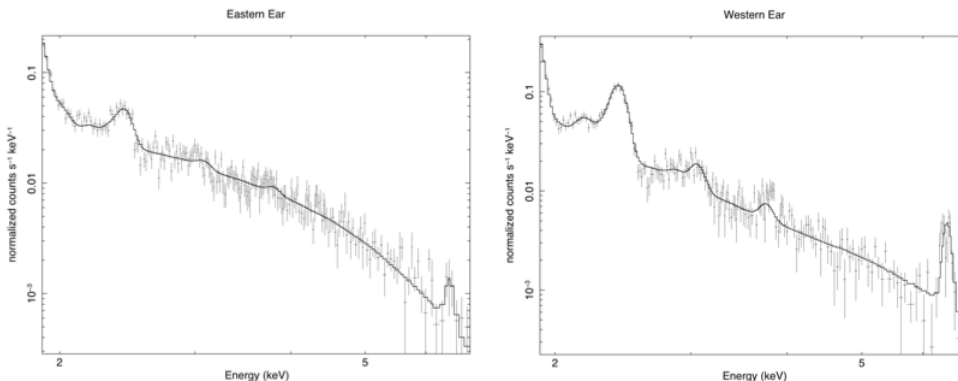


Figure 6: Emission spectra of the eastern and western ears. The differences in the high energy continuum profiles contradict the theory of them being linked on a larger structural level.

The line strengths seen in the emission spectrum of the *eastern ear* are much weaker overall compared to its western counterpart. While the photon count could have been affected by the latter’s proximity to the northern overdensity, this difference in flux cannot account for the large discrepancies at the level of the S and Fe K lines, as seen in Figure 6. Instead, it is more likely that the material comprised within two regions has different elemental abundances.

The argon and calcium emissions that contribute to the spectrum of the *western ear* are lower than what is observed in their line profiles across the entire remnant. Similarly, the sulfur abundance predicted by the fit is also below the one presented in Table 2. Despite the reduced photon count at these energies, there are still clear indications of the emission lines above the continuum. Conversely, the eastern region features barely visible profiles of the argon and calcium lines, with great a reduction in the sulfur and K-shell iron emissions, the most prominent contributors in the 2 – 7 keV range. The overall shape of the high energy continuum across the *eastern ear* resembles a power-law fit. This a clear indication of emission from synchrotron radiation, which has a greater impact on its spectrum as opposed to what can be observed in the western section.

Due to the contrasting nature of their chemical composition, it is doubtful that the formation of the two *ears* originated from a common event. Despite their position at similar radii outside of the material’s spherical symmetry and at opposite ends of a diameter crossing the geometrical center of the remnant, the elemental abundances inferred from the spectral analysis diverge too much from one another in order to suggest a link between the regions. In lack of an instrument that would provide precise depth of field observations for the extended source, it is still possible to speculate the existence of a large scale ring that envelops Kepler and that contains both the eastern and the western *ears*. However, the evidence presented here shows no real connection between the composition of the plasma within the two regions.

### 3.3 Principal Component Analysis

In the previous sections we have focused on identifying and analyzing the chemical composition of Kepler’s SNR by referencing key regions outlined in the object’s x-ray and optical emission. A basic mapping of elemental abundances across the notable features throughout the volume has facilitated several conclusions regarding the structure of the object, as a whole. Nonetheless, more insight into the nature of the remnant can be derived from an in depth investigation of the Chandra dataset via principal component analysis.

The latter defines a set of mathematical procedures that can be applied to multi-variable datasets with the intent of probing for patterns between seemingly independent parameters. The variables are separated into linearly uncorrelated pairs named principal components by extracting those elements that display the highest variance within the entire dataset, subsequently employing these as a new system of coordinates for the remaining variables. At this stage, it is expected that a significant portion of the irregularity contained in the data should already be accounted for. The extraction of an additional pair of principal components takes into account the second highest variance in the data, with the supplementary requirement of it being uncorrelated with the previous pair of factors. Similarly, these elements are also responsible for considerable variability, but would account for less than the first pair. Further principal components will correspond to an increasingly lower variances, with lower and lower contributions brought to the overall irregularity in the dataset.

When applied to the Kepler observations, principal component analysis can be used to reveal correlations between the recorded photon energies across the remnant, confirming patterns between the elemental abundances inside the material. In turn, these correlations can point towards specific physical mechanisms that acted throughout the object’s evolution and that shaped the plasma in its current form.

For the purpose of this study, the first three principal components were chosen to be investigated. This ensures that only those energies that are responsible for the highest variance in the dataset, which also have the highest chance to be correlated, are considered. Additionally,

the scores associated to first three components also correspond to a singular value significance above the 0.1 threshold. The scores and corresponding Kepler images are provided courtesy of Sjors Broersen, Astronomical Institute "Anton Pannekoek".

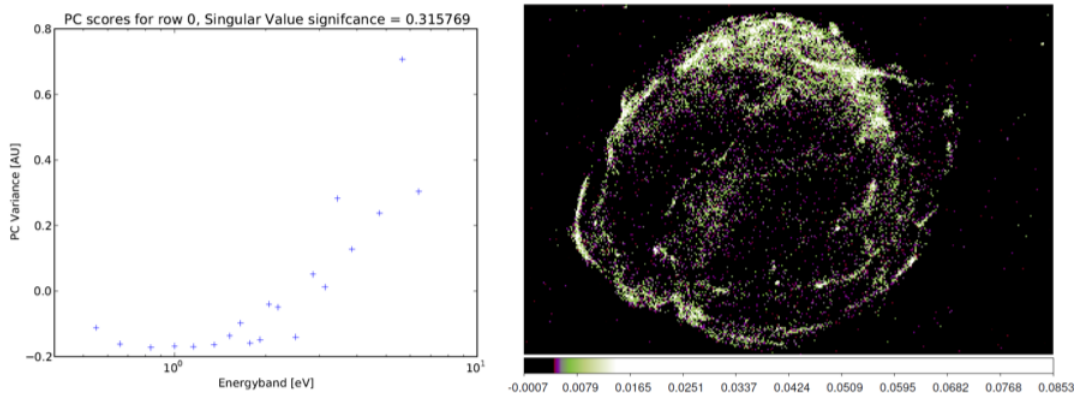


Figure 7: Model corresponding to the first principal component. The image (right) maps the variance plot (left) across the remnant. Bright regions correspond to a higher variance, while dark regions to low variance. The regions extracted with the mask tool are included in the appendix.

The distribution of pixels across the images made it difficult to manually extract relevant bright regions using the DS9 tool. In order to achieve a higher degree of accuracy in the selection process, which would translate into a better representation of the emission spectrum, a series of additional procedures were used on the data contained in the images. Initially, a region containing the remnant itself and little else was separated from the background, such that any pixels not pertaining to the object would be ignored in the subsequent analysis. A smoothing filter was then applied on the selected region. Its overall effect seeks to reduce the impact of individual data points on the entire dataset. Among the advantages of this filter are noise cancellation, as well as minimizing the detrimental effects caused by the different sensitivities of neighboring pixels on the CCD device. Lastly, a mask script was used in order to select the regions of interest from each image.

By inputting convenient values for the upper and lower threshold values, pixels of a specific brightness could be extracted and mapped to a different file. For instances where regions with negative principal component scores needed to be selected, the brightness of the image was inverted. This made previously dark colored pixels bright and easily distinguishable from the background when mapped onto the mask file.

Figure 7 depicts the scores computed for the first principal component. By definition, the projection of the highest variance in the dataset should lie on the first coordinate of this system and should be readily observable in the associated plot. At a first glance, values that significantly exceed the average on the y-axis can be identified in the 4.5 – 6.5 keV range. The peak variance corresponds to an energy of 5.9 keV, with the addition of two neighboring high variance points at 4.8 and 6.5 keV. The first value

falls within the range of the manganese spectral line complex and coincides to a strong degree with the emission peak of this specific element. The image predominantly maps the high variance regions to the northern segment of the remnant, as well as the outer edges in the west and the southwest. Softer traces can be observed sporadically inside the peripheral material and in thin filaments scattered throughout the volume. Aside from small anomalies that amount to very few pixels in total, the central region of the remnant displays little variance. The majority of bright regions are concentrated at larger radii and delimit a roughly spherical shell around the volume. The variance in manganese abundances within these areas can be attributed to the nature of neutron capture mechanisms that are vital to the element’s nucleosynthesis. At the time of the supernova explosion, nuclei with uneven numbers of protons and neutrons become magnets for the free neutral particles released inside the plasma and can fuse into heavier and more stable particles. The stable  $^{55}\text{Mn}$  is a result of a neutron capture process undergone by  $^{55}\text{Co}$  during the incomplete Si burning stage (Badenes 2008).

The half-life of  $^{55}\text{Co}$  is shorter than 18 hours. Manganese can only be synthesized within this timeframe if the Co nucleus is enriched with a neutron before it decays. Due to the random nature of this process, the manganese concentration varies greatly in the outer regions where material was less neutron-rich compared to the one at lower radii. An additional reason behind the presence of the darker central regions displayed in the image revolves around the position of the reverse shock inside the remnant. Most of the material carrying heavier elements was propelled toward the exterior after the supernova explosion, leaving the innermost volume with lower manganese abundances. As the reverse shock travels back toward the center, the plasma mixes and gives rise to variances in chemical composition, especially for elements whose formation depended on the flux of the initial neutron excess. Given the timescale and taking into account the analysis of the Fe L / Fe K line ratio performed in the previous section, it can be assumed that the reverse shock has not travelled far enough toward the central regions in order to perturb the manganese abundances present there.

Parameter	PC Variance $\geq 0.6$
Chromium line flux [ $10^{-13}$ <i>ergs/cm<sup>2</sup>/s</i> ]	$1.60 \pm 0.18$
Manganese line flux [ $10^{-13}$ <i>ergs/cm<sup>2</sup>/s</i> ]	$1.09 \pm 0.29$
$\frac{F_{Mn}}{F_{Cr}}$	$0.68 \pm 0.23$
$\frac{M_{Mn}}{M_{Cr}}$	$1.05 \pm 0.45$

Table 6: Photon flux values associated to the chromium and manganese spectral line complexes. The encompassing spectrum was extracted from the bright regions highlighted by the first principal component analysis. The corresponding spectrum is included in the appendix.

The recorded PC scores indicate a consistent abundance of manganese in the bright regions highlighted in Figure 7. A similar analysis to the one performed for the northern and southern rings in section 3:2 can be approached here, with the intended purpose of confirming the

metallicity values previously derived in this study. Table 6 contains the computed values of the detected photon flux corresponding to the chromium and manganese emission lines for pixels above 0.6 PC variance. The mass ratio value is consistent to the one identified for the

northern ring, due to the fact that a large portion of the region extracted via the mask file corresponds to segments also pertaining to the former. Using the power-law

$$\frac{M_{Mn}}{M_{Cr}} = 5.3 \cdot Z^{0.65}$$

we determine a value of  $Z = 0.082^{+0.061}_{-0.047}$ , which further supports the supersolar nature of the progenitor’s metallicity.

The principal component variance of the neighboring energy range, between 4.5 and 7 keV, averages at approximately half the peak value at 5.9 keV. This discrepancy contradicts the possibility of a correlation between the abundances of Mn and Fe K, which implies that the strong iron line complex present in the spectrum at 6.5 keV is not a suitable tracer for manganese emission. Regions featuring a high variance of the Fe K abundances are predominantly described by thin filaments that are also be predominantly found at the edges of the remnant. The imbalance of K-shell iron emission is caused by local temperature variations that can favor or impede the ionization process. This phenomenon occurs in sections where the hot shocked ejecta material comes into contact with the cooler shocked ambient medium and is well represented by the filaments depicted in Figure 7.

A bright extended region can be observed at an offset of approximately 10” towards the west of the geometric center. At intensities comparable to those in the peripheral areas, this section displays a higher variance in the Fe K abundance without outlining any filamentary structures. Although its occurrence can also be attributed to the mixing the two plasma components, the differences in terms of structure might indicate that a different mechanism is involved. The central region is also prominently highlighted in the analysis of the second principal component. Figure 8 (top) depicts its computed PC scores, as well as the corresponding image of Kepler’s supernova remnant. The contrast was altered in order to better represent both the bright and dark areas and to distinguish them from the background. Unlike the previous principal component, here the scores peak at both

positive and negative values meaning that both very bright and very dark pixels indicate regions of high variance within the volume.

The highest positive value, represented by the bright pixel regions in the image, is recorded at 6.5 keV and corresponds to the emission peak of the Fe K line complex. The thin filaments are replaced by a granular structure that spreads predominantly across the northern and western sections of the remnant, as well as in the region adjacent to the central crossing ring. Overall, the image associated with the second component maps the distribution of the Fe K ejecta across the remnant, with the results being consistent to previous investigations of Kepler. In their analysis of the XMM dataset, Cassam-Chenai et al. have also identified the extent of the ejecta containing K-shell ionized iron as predominant at the shoulder, eastern eye and elbow (Cassam-Chenai et al. 2004). The emission spectrum of the eastern eye, included in the appendix, is of particular note here. The data reveals a relatively high photon count rate across the entire x-ray range compared to neighboring central areas, indicating that this extended region accounts for most of the central emission within the remnant. The fact that the variance map computed for the second principal component would overlap to such an extent to the profile of the eastern eye might indicate a correlation between the abundance of Fe K inside the region and the mechanisms that contributed to its formation.

Although there are indications of strong iron emission in the northern section of the remnant, the brightness profiles seen in Figure 1 do not match those mapped by the second principal component scores. The full extent of Kepler’s remnant is highlighted by the dominant topmost emission, whereas the Fe K ejecta is more evenly distributed throughout the key regions mentioned above. This discrepancy contradicts the possibility that the eastern eye was shaped by the same processes that generated the very bright northern segment, namely the accumulation of material as a result of Kepler’s indicated space motion.

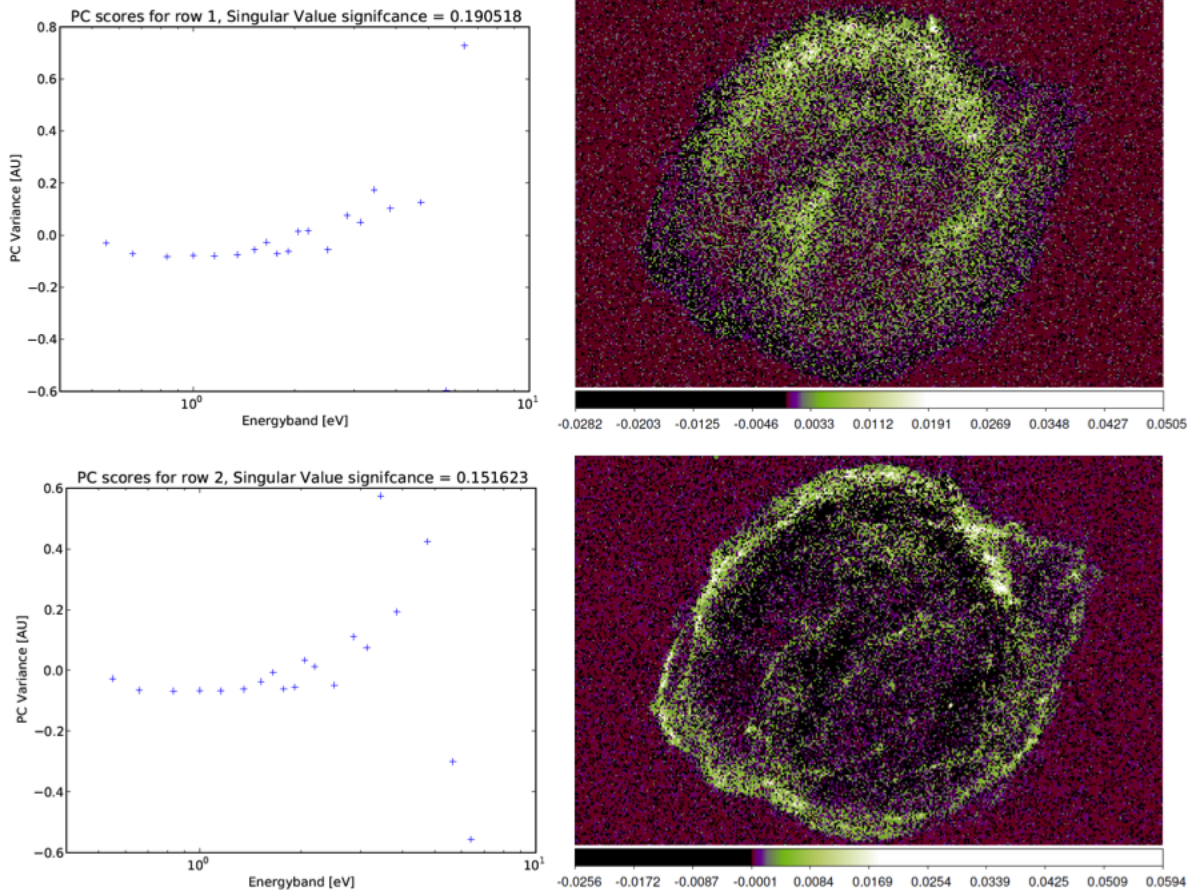


Figure 8: Models corresponding to the second (top) and third (bottom) principal components. The contrast was enhanced in order to reveal both bright and dark pixel regions across the images. The regions extracted with the mask tool are included in the appendix.

The asymmetry of the Fe K ejecta distribution within the remnant can also be caused by interactions with the ambient medium at the time of its expansion. Despite the fact that few variations in the consistency of the ISM are expected at such a high redshift, density variations in the environment could have been induced by the presence of a massive companion star. The position of the eastern eye, close to the geometric center and independent of other asymmetries of the object, brings further arguments in support of this theory. Although the existence of this region is not a clear indication of the single degenerate scenario, in part due to the fact that no trace of the companion star was detected up until this point, this model can explain the correlation between the Fe K distribution and the

overall x-ray emission of Kepler. Throughout its expansion, the ejecta material could have interacted with the circumstellar material of the massive companion, situated at a southwestern offset from the exploding white dwarf. This process can explain the accumulation of the iron-rich plasma in the region of the eastern eye.

The negative peak score corresponds to a value above 5.5 keV. Due to the nature of the principal component sequencing, each added component is defined as uncorrelated to the previous. By defining the second set of data as orthogonal to the first, the variances recorded for the Mn lines no longer contribute to the PC scores. In turn, this causes the regions that

initially represented bright peaks to be appear as darker areas in the subsequent image. This overlap permits a direct comparison between the key regions outlined in consecutive principal component models and provide additional insight into the mechanisms that led to the current element distribution across the remnant.

Figure 8 (bottom) contains the scores recorded for the third principal component. The associated image reveals that the bright regions are mostly situated around the edges of the remnant, with very little additional structure in the innermost 0.8 R of the volume. According to the distribution of the material, it is expected that the emission is dominated by synchrotron radiation produced by the rapid motion of highly energetic particles. The computed spectrum displays the typical high-energy continuum profile associated to this emission, with few notable features above the 4 keV threshold. Nonetheless, the calcium line above 3 keV carries significant strength and is easily observable above the continuum line. This can be correlated to the positive peak of the PC variance plot, which can be found at 3.4 keV, within the energy range associated with calcium x-ray emission. Type Ia supernovae are mainly responsible for the production of iron peak elements, such as Mn, Fe and Ni, and have a reduced contribution in terms of calcium enrichment. Synthesis of the latter element is generally attributed to the alpha processes in type II supernovae, which also give birth to stable Si and S isotopes. Although alpha decay is not a process typically associated to type Ia explosions, some quantities of alpha particles (particles that consist of two bound proton-neutron pairs) could have been introduced into the system via cosmic rays. This effect is localized to the outer shell of the remnant due to the increased density exhibited by the material at high radii. The cooler medium found near the edges is characterized by a higher particle density per unit volume compared to the hotter material in proximity to the reverse shock. The alpha particle is less likely to travel farther away towards Kepler’s geometric center with-

out interacting with the remnant’s material. As such, the highest carbon abundance can be traced to the outer regions, where the absorption of the alpha particle is most common.

The extent of the synchrotron emission across the remnant confirms the results of the comparison between the western and the eastern ear. Therein, it was observed that the emission spectra of the two regions exhibited different line profiles and the elemental abundances predicted by the fitted models were also divergent from one another. The emission attributed to the western ear exhibited strong traces of synchrotron radiation, which is also marked in Figure 8 (bottom) by bright pixels to the southwest. In contrast, the eastern ear displayed strong spectral line features across the high energy continuum. The image resulted from the PC analysis supports this prediction. The majority of this regions shows average variance scores, with very few bright pixels that can be associated to synchrotron emission delimiting its external contour.

The negative PC scores shown as dark pixels in Figure 8 (bottom) outline the Fe K ejecta previously investigated. For the most part, it is layered beneath the synchrotron radiation emissions, with the addition of the extended central region overlapping the eastern eye. By analyzing both of their contributions in tandem and by comparing their distribution across key regions, it is possible to derive structural information regarding the remnant as a whole. The most notable observations concerns the difference between the western and the eastern ear, as important markers of the E-W asymmetry. While the former is dominated by bright pixels, indicative of synchrotron radiation, the eastern section shows significant contributions from the Fe K ejecta. The result enforces the belief that the two ears were not formed as part of a single major structure across the remnant, but are instead the outcome of individual mechanisms that contributed to the expansion of the material through the surrounding environment.

### 3.4 Analysis of Secondary Dataset

The distribution of nickel abundances throughout Kepler’s supernova remnant will be investigated using both the Chandra information, as well as a supporting dataset recovered from the XMM-Newton archives. Given the nature of the emission process and the limitations of the CCD devices, the spectral features above the 7.0 keV threshold prove more difficult to accurately identify and analyze compared to the 0.5 – 6.9 keV range described so far. It is expected that using information provided by two separate devices will yield a better representation of the line complexes found across the high energy continuum. By accounting for each of the instruments’ shortcomings and by capitalizing on their individual advantages, it is possible to obtain a detailed description of the nickel line at 7.5 keV.

The XMM-Newton dataset needed to be calibrated and filtered before a proper emission spectrum could be extracted. This was accomplished by means of the Science Analysis Software (SAS), a set of tools specifically designed for use on the datasets collected with the XMM. The initial pre-processing stage involved the retrieval of appropriate current calibration files, known as CCFs, for the MOS1 mounted atop the EPIC instrument. The layout of the detector is comprised of seven separate CCDs. The calibration files account for the dead spaces between the cameras, which are caused by the separation between detector edges (XMM-Newton Users’ Handbook 2007). This effect heavily impacted the original Kepler image, which revealed a thick dark line intersecting the field of view of the remnant, effectively rendering as many as 10% of the relevant pixels unusable. The calibration nullified this issue and provided a complete picture of the SNR. Subsequently, standard and temporal filters were applied to the dataset in order to account for hindering phenomena such as photon background flaring. The SAS toolset allowed for the extraction of both the source and the background spectrum, as well as building the redistribution matrix and ancillary region file

necessary for the upcoming analysis. These files were input into the SPEX software package. The resulting XMM emission spectrum along with the extended spectrum processed from the Chandra dataset are shown in Figure 9.

Both of the two datasets were fitted with the same two-component *nei* model employed in the previous sections. As it can be observed in the images, the Chandra dataset makes it difficult to identify the profile of the nickel line complex above 7 keV. Although at a lower overall resolution, made evident by the reduced number of data points registered on the plot, the secondary instrument benefits from an expanded field of view that makes it possible to better represent the desired emission range. In case of the Chandra spectrum, fitting the model did not provide an adequate depiction of the line profile. Conversely, the XMM data revealed a well-defined feature peaking at approximately 7.5 keV, well within the expected range of this specific nickel emission. The strength of this feature was comparable to that of the argon and calcium lines that were also prominent components along the high energy continuum range, indicating an important nickel contribution to the overall chemical composition of Kepler’s supernova remnant.

The relevant elemental abundances predicted by the models corresponding to both the Chandra and XMM datasets are listed in Table 7. This representation makes it easier to directly compare the values computed in each separate instance. For the purpose of this investigation, only elements commonly present in the shocked ejecta material were listed due to the specific focus being the high energy continuum range across the complete spectrum. Despite the fact that the analyzed spectrum covered the entire extent of the remnant, the resulting abundances differ slightly from those determined in Section 3.1 due to the fact that different segments of the dataset were included in the fitting process. When probing for the presence of the nickel line, the 0.5 – 1 keV energy range was omitted from the analysis, which altered the contributions of the two iron components and implicitly those of Si, S, Ar and Ca.

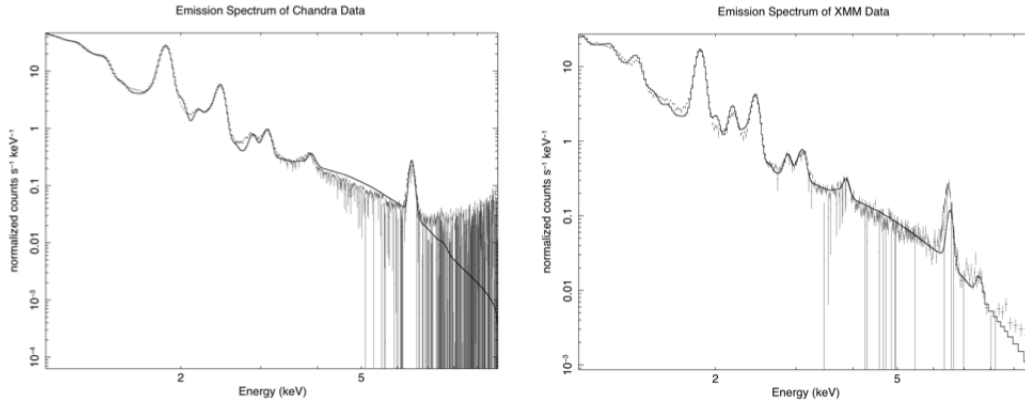


Figure 9: Emission spectra corresponding to the Chandra (left) and XMM-Newton (right) datasets. The extended range permits the investigation of the nickel emission above the 7 keV threshold.

Parameter	Chandra Model	XMM Model
Si	4.51	4.18
S	5.68	5.81
Ar	5.68	5.25
Ca	9.64	8.24
Ni	$\approx 10^{-6}$	7.17

Table 7: Best fit parameters for key elements in the shocked ejecta material whose emissions are recorded in the 2 – 8 keV energy range. The table contains results corresponding to both the Chandra and XMM-Newton datasets.

The abundance values listed for both models correspond to a large extent, with the exception of the nickel parameter. In line with the expectations, in the case of the Chandra observation the two component *nei* model could not account for the presence of a nickel line complex beyond 7 keV, due to the nature of the data points above that energy threshold. The continuum exhibits a steady drop off, interrupted only by a faint feature at a location equivalent to the nickel emission. On the other hand, the model fitted to the XMM dataset is able to outline a strong profile of the spectral line, as well as provide a feasible estimate for the element’s abundance throughout the entire remnant.

The importance of acknowledging the nickel content inside Kepler’s SNR is twofold. Firstly, estimating its current abundance can broaden our perception of the remnant’s early evolution, both in terms of structure and chemical composition. The decay processes that are involved in the element’s nucleosynthesis shortly after the supernova explosion release certain amounts of energy that contribute to its bright emission for a period of several weeks. As a result, there is a strong correlation between the amount of stable nickel isotopes produced during this stage and the recorded duration of the supernova’s fade out. Kepler is said to have been visible for a period exceeding twenty days, although the technological limitations of the era made the determination of an exact timeframe impos-

sible. Nonetheless, by tracing its nickel abundance and by comparing its value with those of recently observed type Ia remnants of similar size and origin, it is possible to more accurately discern this interval. In turn, this fade out duration can be further correlated to other processes involved in Kepler’s early evolution and which carry valuable insight into the nature of the remnant’s progenitor system.

Moreover, the transition from the unstable  $^{56}\text{Ni}$  isotope to the stable  $^{56}\text{Fe}$  is also reliant on the density of free neutrons and electrons in the material shortly after the supernova explosion. Within a timespan below 60 hours,  $^{56}\text{Ni}$  undergoes a beta decay process and is converted into  $^{56}\text{Co}$ . If, within this interval, the nucleus is able to capture and affix an additional neutral nucleon, it can evolve into a stable form of  $^{58}\text{Ni}$ . The odds of this occurring are correlated to the free neutron flux released through the plasma. It is estimated that 68% of all stable nickel is in the form of  $^{56}\text{Ni}$  (Pagel 2009), whereas 50% of the total iron content in supernovae is provided by  $^{56}\text{Fe}$  (Nomoto et al. 1997). These approximations make it possible to comparing the current abundances of nickel to those of the iron found in the remnant, which in turn can enable us to discern a measure of the neutron flux emitted during the explosion.

## 4 Discussion and Conclusions

This study was aimed at investigating the relative abundances and distribution of key elements across Kepler’s supernova remnant, with the intended goal of uncovering additional information regarding the evolution mechanisms that acted upon the object. The main dataset used throughout the analysis, taken from the Chandra observatory database, consists of six separate observations merged into one single event file list. For key regions of the remnant, emission spectra of the 0.5 – 7.0 keV energy range were extracted and processed via dedicated software tools.

Initially, the full extent of the plasma visible in the x-ray band was investigated. The spectrum was fitted with a two-component model that could distinguish between the contributions of the shocked ambient medium and the shocked ejecta material, as well as determine abundance estimates for the elements most prominently displayed on the spectrum. Brief comparisons with other known type Ia supernovae have revealed matching profiles of the sulfur, silicon and argon lines. However, notable discrepancies were observed with regards to the two major iron emission contributors within the energy interval. By comparison to the Fe L line complex seen in Tycho’s SNR, the one observed in Kepler is much more prominent and has a more convoluted structure, signifying an overall greater allotment of the shocked ambient medium material within the plasma volume. Moreover, the emission of the K-shell ionized iron displayed a sharper peak at the far end of the spectrum compared to the one in SNR 0519-69, a type Ia remnant detected in the Large Magellanic Cloud. This indicates that the temperature profile of Kepler extends to higher values by comparison, a statement which is also supported by the difference in size between the two objects.

A comparison between the individual strengths of the Fe L and Fe K lines was also performed. Starting from the assumption that L-shell transitions require an overall lower  $T$  to occur than K-shell ones, a coarse gradient of the temperature distribution across the remnant was determined. In order to accomplish this, the volume of the remnant was divided into ten concentric areas, each at an increment of  $R/10$  greater than the previous. Subsequently, values of the Fe L / Fe K ratio were computed for each region individually. The lowest results were recorded within  $0.4 - 0.7R$ , with a very narrow gradient delimiting the adjacent areas. These values were associated with the peak of the temperature profile. According to the theory behind type Ia structure and composition, the distribution of temperature values within the plasma is closely related to the position of the reverse

shock traveling inwards, toward the geometric center of the object. The cool material at the center grows progressively hotter as it nears the reverse shock and cools down once more near the edges of the remnant. These considerations were in line with the results of the iron line ratio analysis, with the exception of the  $0.9 - 1.0R$  region that displayed an anomalous value far exceeding the expectations. This inconsistency was most likely induced by the rough selection of material near the outer edges. Discounting this result, the line ratio distribution points towards the position of the reverse shock somewhere within the  $0.4 - 0.7R$  interval.

Despite its spherically symmetric outline, Kepler’s supernova remnant displays several structural irregularities visible both in its optical and x-ray emission. Previous studies had already delimited the notable features seen in the observations and had traced a number of axes of symmetry across the remnant. Individual emission spectra were extracted for several of these key regions. This facilitated the investigation of their chemical composition by focusing on the energy ranges of the most prominent spectral features, such as the Si, S, Ar and Ca lines. In doing so, it was possible to probe for connections between seemingly independent structures and to discern the processes that were behind their formation. The occurrence of the eastern and western ears, two features situated near the edge of the remnant in a position diametrically opposite to one another, is the most noteworthy instance of breaking the overall spherical symmetry of the object. As a result of their relative location, it was possible that the two had emerged from the same evolution mechanism and that they were part of a larger structure stretching across the whole body of the remnant. Nonetheless, by comparing the elemental abundances modeled onto their emission spectra, it was determined that the material present inside the two regions had very few common properties. The eastern ear featured an important contribution of the Fe K ejecta, while the high energy continuum of the western ear was dominated by synchrotron

radiation and displayed weaker argon and calcium lines above the 2 keV threshold.

A specific focus was also allocated to manganese and chromium emissions from the shocked ejecta material. A previous x-ray investigation of type Ia remnants has successfully correlated the flux ratio of these two elements to the metallicity of the progenitor star, with an application to Tycho’s SNR. Following the guidelines presented therein, a result of  $Z = 0.082^{+0.061}_{-0.047}$  was determined. Much like in Tycho’s case, these values point toward a solar or supersolar metallicity of the progenitor.

An in depth analysis of the first three components of the PCA analysis allowed a more precise determination of the Fe K ejecta distribution across the remnant, as well as outlining the extent of the synchrotron radiation’s influence on the peripheral areas. The location of the eastern eye, one of the most prominent x-ray emitting features near Kepler’s geometric center, was correlated to the peak of the Fe K emission, as dictated by the variance scores of the analysis. Other major contributors were found across the northern overdensity and in proximity of the elbow, to the southeast of the remnant. A correlation between the abundance of manganese and that of the iron in the shocked ejecta could not be confirmed. Despite the fact that the formation of both elements require similar ionization temperatures, the overall sensitivity of the manganese synthesis process to the free neutron flux in the early stages of the supernova make it difficult to trace this element to any other chemical component.

The principal component analysis also revealed a considerable calcium contribution near the edges of the remnant, above  $0.8R$ . Although large quantities of the element are not typically synthesized in the reactions taking place inside type Ia supernovae, it was conveyed that these abundances could have resulted from the influence of cosmic rays that have introduced free alpha particles to the material. Calcium was mainly identified solely at such high radii because these particles were unlikely to have

travelled deeper into the plasma without experiencing interactions with other particles in the surrounding environment.

The Chandra dataset did not permit a feasible determination of the nickel abundance parameter associated to its emission above 7.0 keV. To account for this fact, an additional dataset corresponding to an XMM-Newton observation of Kepler's SNR from 2001, was also employed. Although the overall resolution of the XMM instruments was lower than the one provided by Chandra, the expanded field of view accommodated by the seven CCDs that comprise the MOS1 detector enabled the analysis of the spectrum at higher energies. The two component model used in the previous stages of the investigation was fitted to the relevant emission range and used to determine an estimate of the

nickel abundance across the entire volume of the object.

SN1604, Kepler's supernova remnant is currently one of the most well-documented type Ia representatives in astronomy. During the past few centuries, its extended study has allowed the scientific community to discern relevant information into the exotic processes that govern the formation and evolution of such rare events. However, there is still significant insight to be gained from further exploration of the remnant and with the advent of new and more refined technology, previously elusive avenues of research are opened up. The high quality x-ray observations provided by Chandra and XMM-Newton were paramount to this investigation, which joins the many others in the past and the several still to come in the near future.

## References

- Badenes, C. The end of amnesia: a new method for measuring the metallicity of type Ia supernova progenitors using manganese lines in supernova remnants, 2008
- Bandiera, R. On the origin of Kepler's supernova remnant, 1987
- Bandiera, R. A survey of optical knots in Kepler's SNR, 1991
- Bandiera, R. Subarcsecond structures in Kepler's SNR, 1991
- Behar, E. The Chandra Iron-L X-ray line spectrum of Capella, 2008
- Blair, W. Kepler's Supernova Remnant: the view at 400 years
- Cassam-Chenai, G. XMM-Newton observation of Kepler's supernova remnant, 2004
- Chiotellis, A. Progenitor's signatures in type Ia supernova remnants, 2011
- Cowan, J. Stellar abundances: the r-process and supernovae
- Cowan, J. & Thielemann, F. R-process Nucleosynthesis in supernovae, 2004
- Edwards, Z. The Progenitor of the Type Ia Supernova that created SNR 0519-69.0 in the Large Magellanic Cloud, 2012
- Gondoin, Ph., Users Guide to the XMM-Newton Science Analysis System, Issue 9.0, 2012 (ESA: XMM-Newton SOC).
- Kramida, A., Ralchenko, Yu., Reader, J., and NIST ASD Team (2012). NIST Atomic Spectra Database (ver. 5.0), [Online]
- Nomoto, K. Nucleosynthesis in type Ia supernovae, 1997
- Pagel, B. Nucleosynthesis and chemical evolution of galaxies, 2009
- de Plaa, J., Ebrero, J., Grange, Y., Pinto, C., Kaastra, J. SPEX Cookbook, 2010, [Online]
- Podsiadlowski, P. The progenitor of SN 1987A, 1992
- Reynoso, E. A new determination of the distance to Kepler's supernova remnant, 1999
- Sarazin, C. X-ray emissions from clusters of galaxies, 2008
- Snowden, S., Valencic, L., Perry, B., Arida, M. The XMM-Newton ABC Guide: An Introduction to XMM-Newton Data Analysis 2011, [Online]
- Timmes, F. On variations in the peak luminosity of type Ia supernovae, 2003
- Townsley, D. Evaluating systematic dependencies of type Ia supernovae: the influence of progenitor  $^{22}\text{Ne}$  content of dynamics, 2009
- Vink, J. Supernova remnants: the X-ray perspective, 2011

## Appendix

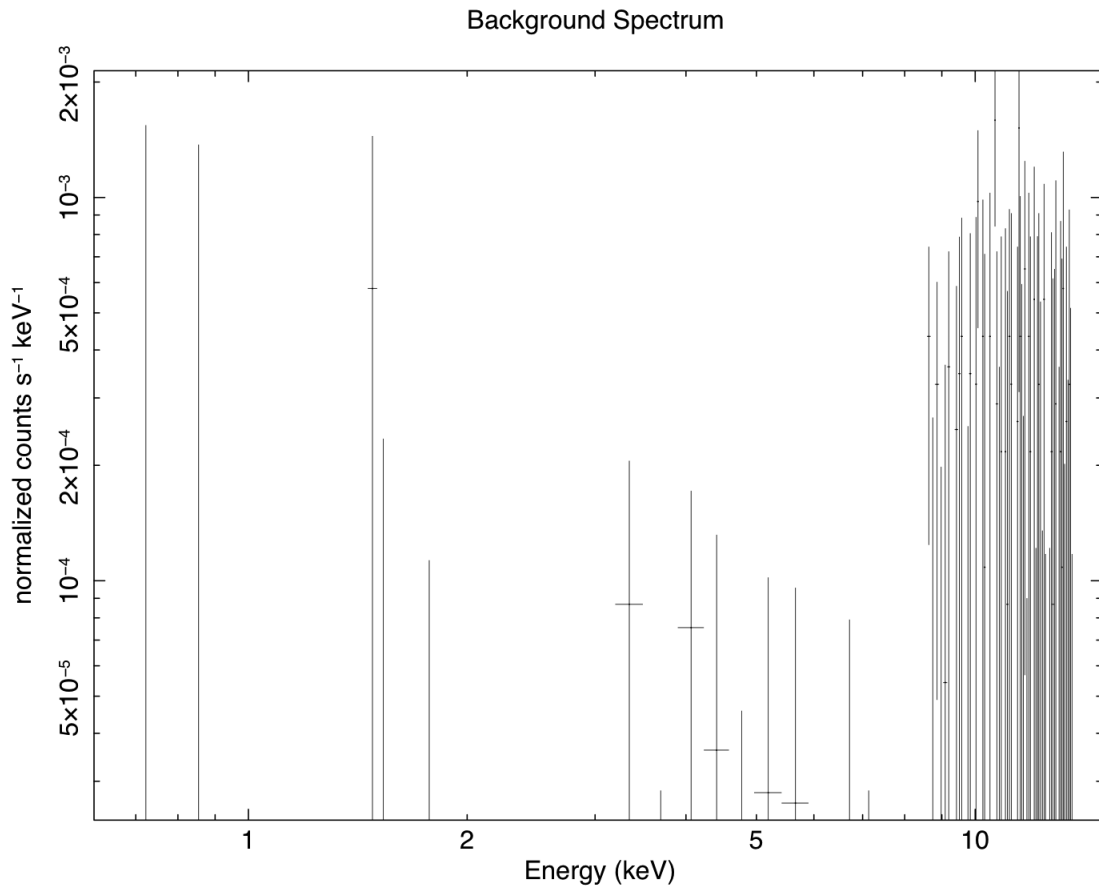


Figure 10: Background spectrum extracted from Chandra’s observation of Kepler’s SNR. The spectrum corresponds to three regions in proximity of the object, within 200” of its geometric center. These regions describe circles of 10” in diameter.

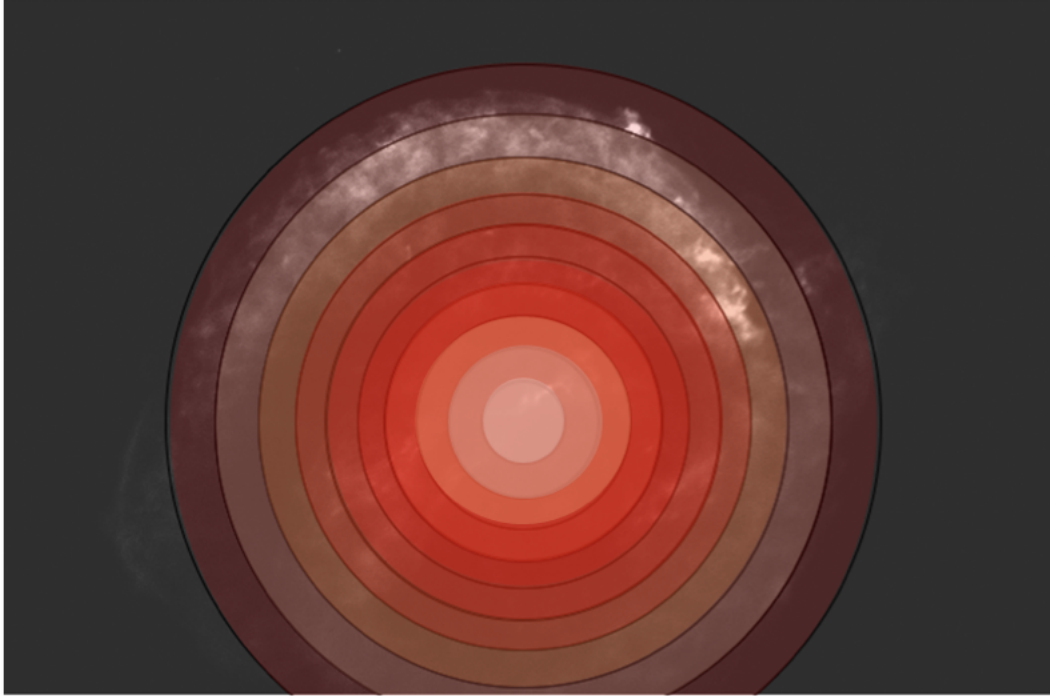


Figure 11: Distribution of the Fe L / Fe K ratio across the radial profile of the remnant. A singular value of the ratio was computed for each of the ten marked regions. The color describes the temperature of the plasma inside the specific regions, as dictated by Fe L / Fe K. The hottest material, which can be correlated to the position of the reverse shock, is found within  $0.4 - 0.7$  R. A more accurate determination is impossible due to the gentle slope of the gradient that characterizes these regions. The anomaly in  $0.9 - 1.0$  R, where the plasma appears hotter than in the previous regions, is attributed to the asymmetric distribution of material at the edges of the remnant.

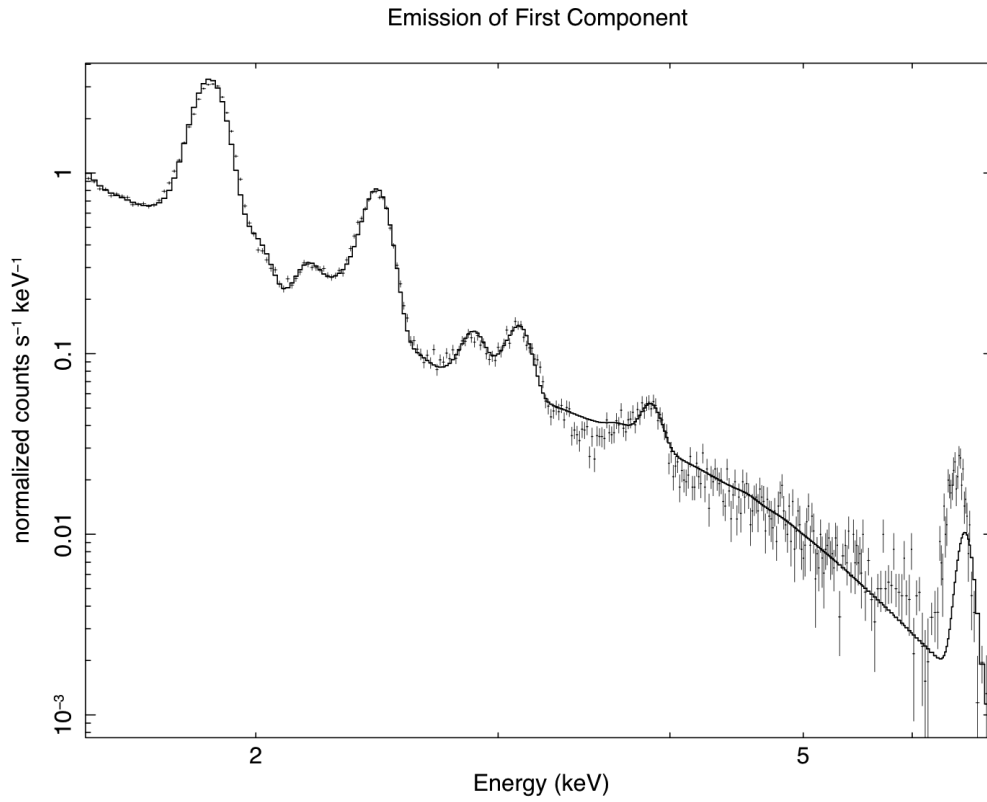


Figure 12: Emission spectra corresponding to the regions highlighted by the first principal component analysis. A strong manganese line profile can be discerned at 5.8 keV.

Parameter	Abundance
Si	2.70
S	2.99
Ar	3.49
Ca	3.42
Fe	4.31

Table 8: Abundances of elements found in the shocked ejecta material associated to the spectrum in Figure 12.

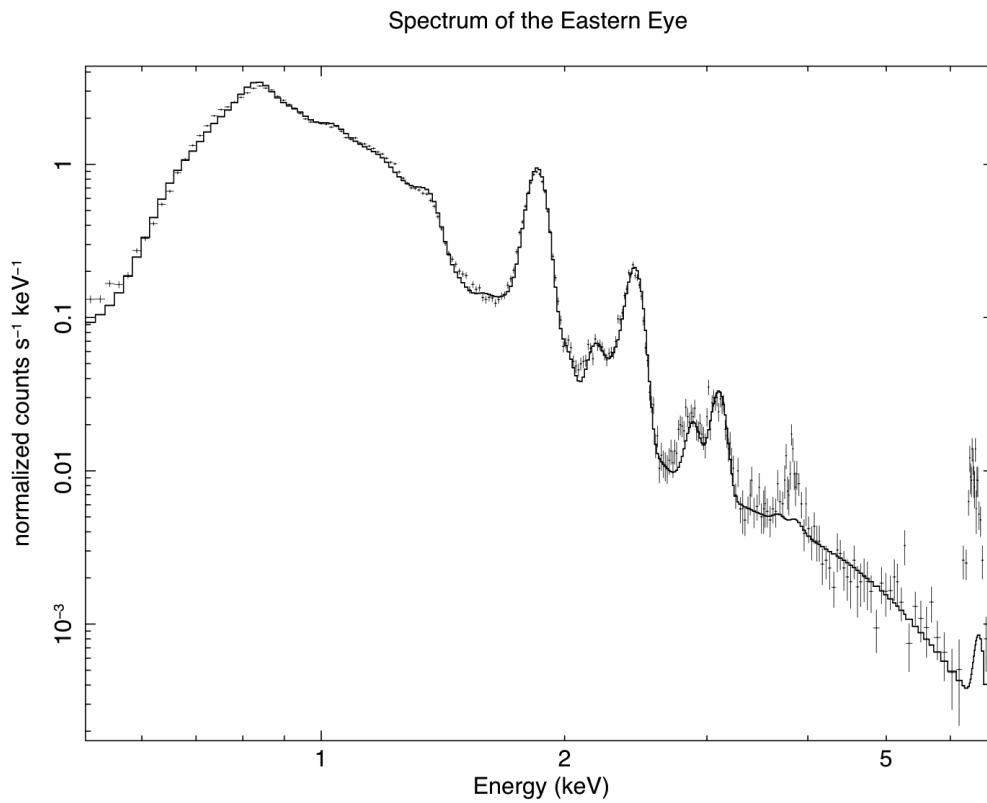


Figure 13: Emission spectra of the eastern eye region overlapping the peak of the Fe K ejecta distribution. Despite the relatively low number of data points that hindered the fit, a sharp Fe K peak is evident at 6.5 keV.

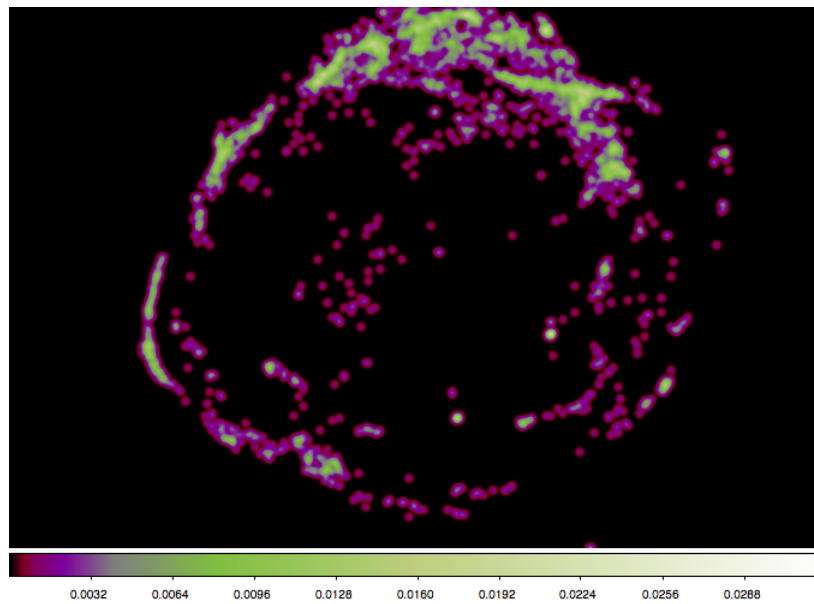


Figure 14: Bright regions pertaining to the first principal component, as shown in image 7. In order to select a proper number of pixels, a cutoff intensity threshold of 0.09 was used as a criterion for the mask tool.

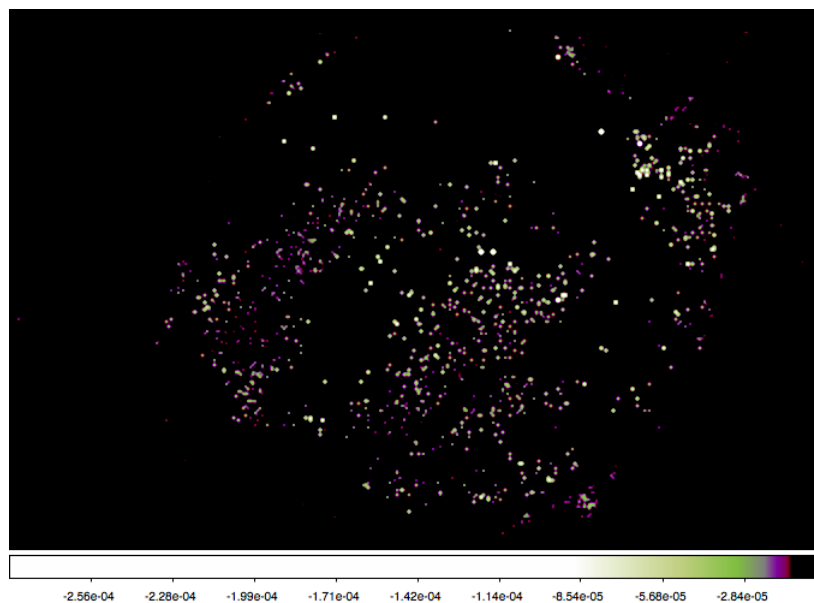


Figure 15: Selection of the dark pixels corresponding to the first principal component. All negative value pixels were extracted using the mask tool. The image uses an inverted colormap.

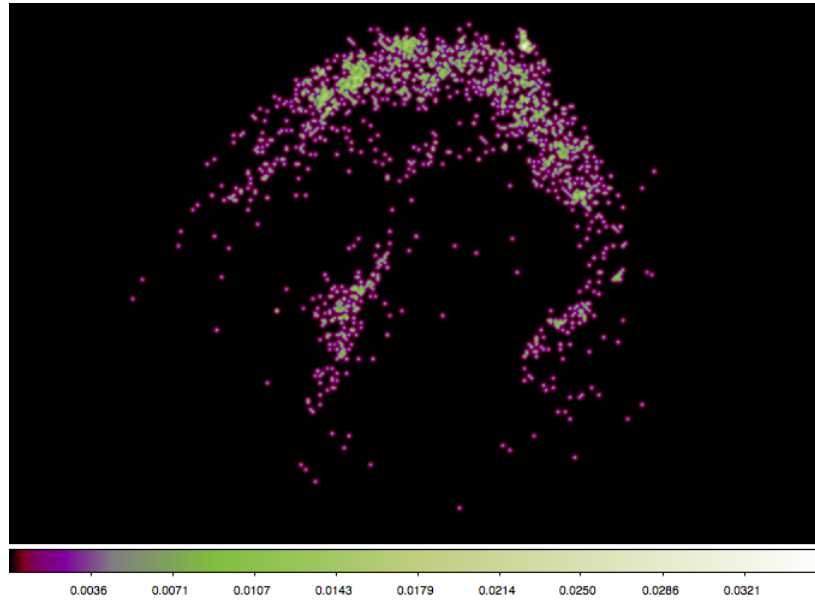


Figure 16: Bright regions revealed by the analysis of the second principal component. To ensure that a sufficient amount of pixels were taken into account for the spectral analysis, the cutoff intensity threshold was lowered to 0.07.

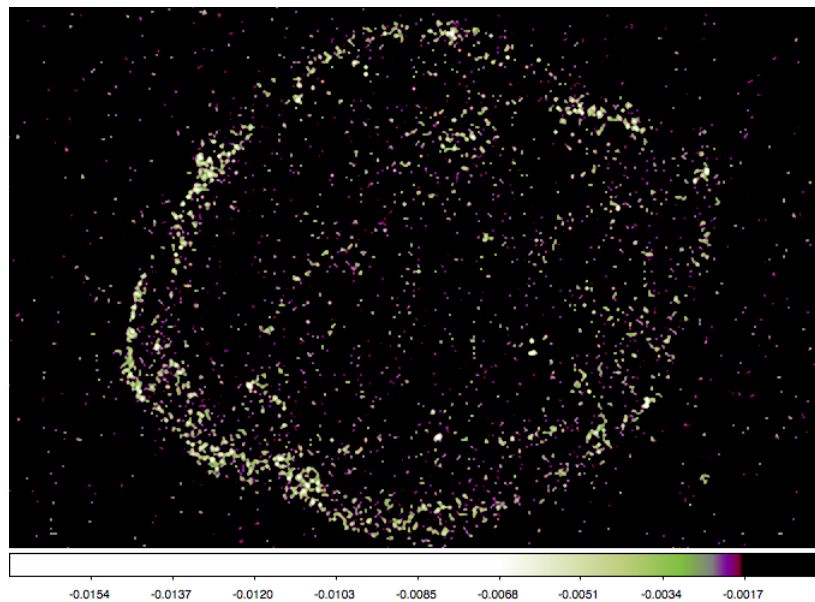


Figure 17: Structure defined by the dark pixels in Figure 8 (top), belonging to the third principal component model. All negative value pixels were extracted using the mask tool. The image uses an inverted colormap.

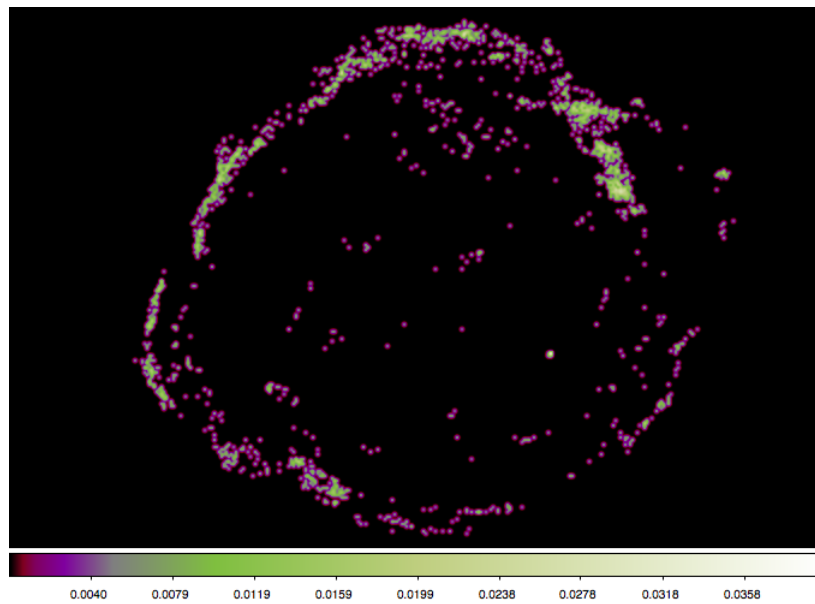


Figure 18: Regions of high recorded variance corresponding to the third principal component, Figure 8 (bottom). The cutoff intensity threshold was set at a value of 0.07, similar to the previous component.

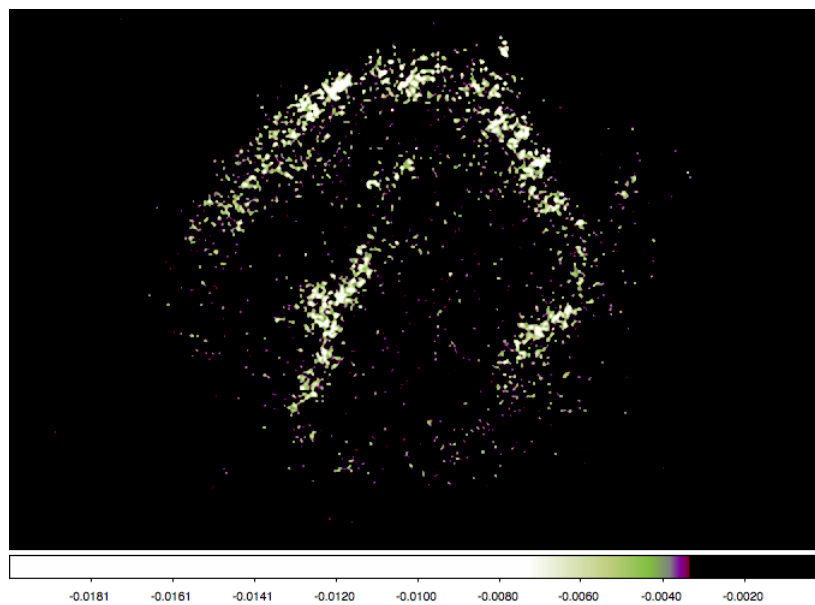


Figure 19: Selection of the dark pixels corresponding to the third principal component. All negative value pixels were extracted using the mask tool. The image uses an inverted colormap.